11-5-2020

Quantitative Analysis and Monte Carlo Modeling of Fat-Mediated MRI Relaxation

Utsav Shrestha

QUANTITATIVE ANALYSIS AND MONTE CARLO MODELING OF FAT-MEDIATED
MRI RELAXATION

by

Utsav Shrestha

A Thesis

Submitted in Partial Fulfillment of the

Requirements for the Degree of

Master of Science

Major: Computer Science

The University of Memphis

December 2020

Acknowledgements

Abstract

Shrestha, Utsav M.S. The University of Memphis. August 2020. Quantitative Analysis and Monte Carlo Modeling of Fat-Mediated MRI Relaxation. Major Professor: Dr. Nirman Kumar.

Hepatic steatosis is the accumulation of fat in the liver, affecting about 25% of the world population. Steatosis can cause lipo-toxicity and eventually lead to fibrosis, cirrhosis and ultimately liver failure if timely interventions are not provided. So, early diagnosis and disease monitoring of steatosis is crucial to reduce morbidity and mortality. Chemical shift based Magnetic Resonance Imaging (MRI) techniques using single and dual R_2^* (transverse relaxation rate) models have been reported to quantify fat fraction (FF) for assessment of steatosis. However, there is no common consensus between these two models and current data is limited for which model is accurate to quantify FF. Fully characterizing the behavior of the models over the entire clinical range of hepatic steatosis is essential to determine the limits of each of the models. However, performing a systematic investigation of the R_2^* models in patient population is infeasible. This thesis presents a computational approach by building a Monte Carlo based model as an alternative way to examine the R_2^*-MRI models.

A 3D liver volume with impenetrable fat spheres was simulated to mimic hepatic steatosis. The simulation of steatosis was done using realistic data obtained from automatic segmentation and characterization of fat droplets using liver biopsy images. MRI signals were synthesized in the virtual liver volume using Monte Carlo modeling approach. Finally, the R_2^* behavior was analyzed using both the single and dual R_2^* models and they were compared against in-vivo calibration to determine their accuracy. Predicted R_2^* values were within confidence bounds of the published in vivo calibration and single R_2^* model showed higher accuracy than dual R_2^* model to estimate FF.

In conclusion, this research developed a computational framework for creating realistic hepatic steatosis model and synthesizing MRI signal and analyzing R_2^* behavior in the presence of fat. The developed computational methods will also be generalizable to create other tissue-specific models and study R_2^* behavior at higher field strengths, for testing new MRI pulse sequences and in presence of other co-existing pathologies such as hepatic iron overload.

Table of Contents

List of Figures

Key to Symbols or Abbreviations

ARMA	Auto Regressive Moving Average
BA	Bland-Altman
CI	Confidence Interval
CT	Computerized Tomography
FD	Fat Droplet
FF	Fat Fraction
FWT	Fat Water Toolbox
GDF	Gamma Distribution Function
MRI	Magnetic Resonance Imaging
NAFLD	Non-Alcoholic Fatty Liver Disease
NASH	Non-Alcoholic SteatoHepatitis
PDFF	Proton Density Fat Fraction
SD	Standard Deviation
TE	Echo Time

Chapter 1 Introduction

Overview

Hepatic steatosis is the accumulation of fat in the liver, affecting about 25% of the world population [1]. Steatosis can cause lipo-toxicity and eventually lead to fibrosis, cirrhosis and ultimately liver failure. As steatosis is reversible condition, early diagnosis and disease monitoring is crucial to reduce morbidity and mortality. Liver biopsy is the current gold standard for the assessment of steatosis. However, biopsy is invasive, painful and suffers from sampling error [2]. In recent years, Magnetic Resonance Imaging (MRI) has evolved as a noninvasive alternative to biopsy for diagnosis of hepatic steatosis [3-5]. Chemical shift-based MRI techniques that incorporate MRI transverse relaxivity (R_2^*) have been reported to quantify Fat Fraction (FF) for assessment of steatosis. [6-8]. There are two R_2^* models based on this technique: single R_2^* model which considers common R_2^* for fat and water and dual R_2^* model which uses different R_2^* for fat and water. There is no common consensus between these two models and current data is limited for which model is accurate to quantify FF. It may not be feasible and can be expensive as well as time-consuming to analyze these models over entire clinical range of FF using patient cohort.

This thesis investigates a computational approach as an alternative way to simulate hepatic steatosis, synthesize MRI signal and analyze MRI relaxivities for determining an accurate model for the quantification of steatosis. An outline of this study is shown in Figure 1. The main components of this research are:

1. To design an algorithm for automatic segmentation of Fat Droplets (FDs) and quantification of FF from liver histology images.

2. To statistically model distributions for the properties of FDs (radius, nearest neighbor (NN) distance and regional anisotropy) from the segmented images for building a virtual steatosis model.

3. Finally, to synthesize MRI signal in the simulated hepatic steatosis volume using Monte Carlo modeling and analyze the R_2^* behavior using both R_2^* models to determine their accuracy.
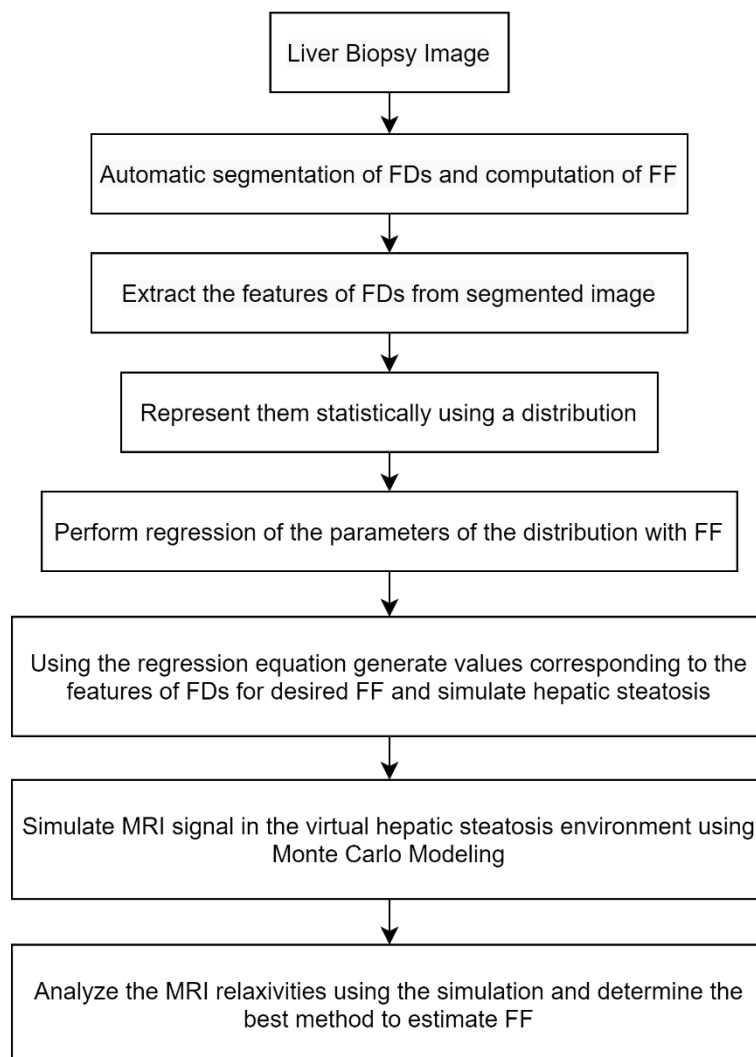
Figure 1-1. An overview of the project

Monte Carlo modeling

Monte Carlo modeling is a computerized mathematical method that applies repeated random sampling rather than using single average value to produce an outcome. It works by constructing a mathematical model of the problem under consideration then runs the simulation for any uncertain aspects of the model. The simulation of MRI signal depends upon water proton's mobility in liver, magnetic field inhomogeneities and the effects of radiofrequency pulses. These form the building blocks of Monte Carlo simulation. Particle size and distribution of FDs extracted from liver biopsy images can be incorporated into the Monte Carlo model to produce realistic magnetic field inhomogeneities. To simulate the diffusion of water protons, the model can use statistical descriptions of proton movement (such as diffusion tensor) or simply assume isotropic diffusion in 3D. The phase accumulated by different proton paths while moving freely in the tissue environment can be used to mimic the MRI signal. Hence, Monte Carlo modeling breaks down complicated physical systems into many smaller sub problems and has been beneficial in simulating and studying various MRI experiments [9-12].

Specific aim and Significance

The primary aim of this project is to understand the underlying mechanisms of fat-water proton interactions in hepatic steatosis by using Monte Carlo modeling. For this, we aim to create a computer program for automatic segmentation and characterization of FDs from liver histology images and build a steatosis model using the characteristics of FDs. The secondary aim of this research is to simulate MRI signal using Monte Carlo modeling and test the robustness of this model by comparing the model predicted relaxivities with the in-vivo calibration.

The success of this project will help build realistic tissue specific steatosis model. Moreover, it will aid to understand the fat-mediated relaxivity in tissues and determine an accurate model to

quantify FF for non-invasive assessment of steatosis. The developed computational methods will also be generalizable to create other tissue-specific models and study R_2^* behavior at higher field strengths, for testing new MRI pulse sequences and in presence of other co-existing pathologies such as hepatic iron overload.

Working Hypothesis

Given the size and distribution of FDs, Monte Carlo modeling will be able to simulate MRI signal in presence of fat and R_2^* behavior can be investigated using multi-spectral fat-water R_2^* signal models.

Outline

Chapter 2 discusses about fat metabolism in human body, how excess fat gets stored in liver leading to hepatic steatosis and then explains the causes, effects, diagnosis and treatment of hepatic steatosis. In addition, it introduces MRI principles and describes about how the presence of fat affects the MRI signal and the limitations of current signal models.

Chapter 3 describes the image acquisition from liver histology slides and the development and implementation of an algorithm for automatic segmentation and characterization of FDs.

Chapter 4 derives statistical models for describing the size and distribution of FDs with respect to FFs and builds a virtual hepatic steatosis model.

Chapter 5 describes the generation of MRI signal from the virtual steatosis model using Monte Carlo modeling, analyzes the R_2^* models and compares the predicted R_2^* behavior to in vivo R_2^*-FF calibration.

Chapter 6 concludes the thesis by discussing the contributions and findings of this project and presents some future prospects.

Chapter 2 Hepatic Steatosis and MRI

Fat Homeostasis

This section discusses about the fat cycle in human body and is intended to discuss how excess fat gets accumulated in liver. Fat is a major source of energy in the human body. Triglyceride is the main type of fat acquired from food sources and fat can store more than double the energy content of carbohydrates or proteins [13]. Triglycerides are also synthesized by adipocytes or hepatocytes. Fat in the form of phospholipids, triglycerides and cholesterol is a major constituent of cell membrane. Omega-(n)3 and docosahexaenoic acid (DHA) are major forms of fatty acid found in the membrane of brain and retina [14]. Also, fat is a transporter of fat-soluble vitamins A, D, E and K to the intestine where they are absorbed. Fat deposits help to insulate the human body and shield vital organs.

According to U.S. Department of Agriculture 2015-2020 dietary guidelines, daily diet for an adult can contain up to 35% of total calories from fat per day which is about 77 grams of fat per day. Blood glucose level rises after eating which triggers pancreas to produce insulin. Insulin is the hormone that regulates the operation of liver. After the production of insulin, body starts to absorb glucose from the blood. In response to increase in insulin, the liver starts absorbing glucose and packages them into bundles to form glycogen. As the glucose level drops, pancreas stops producing insulin. This signals the liver to decompose its stored glucose and send it back to the blood. This helps the body to maintain energy between meals and overnight.

If the liver is full of glycogen, the absorbed glucose is converted to fatty acids by the liver which acts as a long-term storage of energy. The fatty acids are transported around the body via blood which are absorbed by fat tissues. Sometimes, the liver ends up accumulating fat while

producing and storing the extra fat instead of sending it to fat cells. This condition is known as Non-Alcoholic Fatty Liver Disease (NAFLD).

When excess fats are produced or ingested and stored in fat cells then people become obese. According to study, 51% of the population will suffer from obesity by 2030 [15]. Obesity can trigger bone-thinning osteoporosis and heart disease risk. Moreover, it can lead to insulin resistance and type 2 diabetes [16].

Hepatic Steatosis

This section discusses about the causes, effects as well as diagnosis and treatment techniques of hepatic steatosis. Its main purpose is to understand the severity of the disease and why a proper diagnosing method is required for the disease.

Causes and Prevalence

Hepatic Steatosis is the accumulation of fat in liver where at least 5% of the hepatocytes contain fat vacuoles. It is mainly associated with insulin resistance, obesity and high levels of fat (triglycerides) and sugar in blood. In addition, fatty liver is also seen in Drug-Induced Liver Injury (DILI) [17] and is also confirmed as a side-effect of cancer chemotherapy [18,19]. Based on the cause, it can be divided into: Alcoholic Fatty Liver Disease (AFLD) and NAFLD. Approximately 25% of the world population is being affected by NAFLD ([1] .

Types of Steatosis

Morphologically, steatosis can be categorized into two major groups:

1. Macrovesicular steatosis

Macrovesicular steatosis (a.k.a. macrosteatosis) is when Fat Droplets (FDs) are large enough to be able to displace the nucleus and organelles of hepatocytes to the cell periphery. There is

6

only one FD per hepatocyte. It primarily occurs in NAFLD. In addition, macrovesicular steatosis is a primary source of MRI signal in patients with steatosis [20].

2. Microvesicular steatosis

Microvesicular steatosis (a.k.a. microsteatosis) occurs when FDs are tiny, and they accumulate to provide a foamy appearance to the cytoplasm without shifting the nucleus. It is mainly associated with AFLD [21]. In later stage, the tiny FDs of microsteatosis combine with each other to form larger FDs resulting in macrosteatosis.

Effects

Hepatic Steatosis, if not treated on time, can cause liver scarring which is known as liver fibrosis. With time, liver fibrosis will develop into cirrhosis which is life threatening and irreversible. Cirrhosis related to NAFLD is predicted to be the top sign for liver transplantation in the USA in next two decades [22]. If NAFLD is accompanied by liver inflammation, then it is known as nonalcoholic steatohepatitis (NASH), which can lead to cirrhosis and liver failure. About 50% of patients have NASH and 19% have cirrhosis along with NAFLD at the time of diagnosis [23].

Treatment

Although hepatic steatosis is the most common liver disease in the US, no FDA guidelines or approved pharmacologic agents are available yet. There is active research going on in this field and some of them are:

1. Weight loss: It is a natural way to counter hepatic steatosis. It helps to lower insulin level in blood [24]. Several studies have been conducted reporting decrease in hepatic steatosis by weight loss [24-26].

2. Bariatric surgery: Bariatric surgery [27] has proved to be successful in the treatment of hepatic steatosis by multiple research studies [28-30] but its durability is yet to be determined.

3. Orlistat: It is a technique for weight loss by reducing fat absorption. Successful reversal of fatty liver using orlistat has been documented in multiple studies [31,32]. The major side effects of this procedure are gas and bloating.

4. Sibutramine: Like orlistat, it helps in weight loss by decreasing appetite. Experiments have been conducted using this method and decreased evidence of hepatic steatosis has been found [31]. It has similar side effect to orlistat.

5. Pharmacological therapy: There are several pharmacological therapies available to cure hepatic steatosis. Some of them are: Thiazolidinediones, rosiglitazone, Metformin, Statins, fibric acid derivatives (such as Gemfibrozil), etc. Currently, statins are used for the treatment of NAFLD [23].

Diagnosis

The major methods to diagnose hepatic steatosis are:

1. Liver Biopsy: It is the process of extracting sample of liver tissue by inserting a needle into the liver. It is the current gold standard to access hepatic steatosis. In liver biopsy, FDs have a distinct characteristic of white round structure. However, it is invasive and suffers from sampling error as well as interobserver variability.

2. Ultrasound: Liver ultrasound is a non-invasive technique to detect hepatic steatosis. It is currently the most accessible and inexpensive method for the purpose. In the presence of hepatic steatosis, liver appears brighter than the surrounding organs (renal cortex and spleen). It also causes attenuation of ultrasound waves [33]. However, the accuracy of ultrasound depends upon operation parameters and is less sensitive if steatosis is less than 30% [34]. In

addition, the quantification of steatosis can be affected by the heterogeneity in NAFLD patients.

3. Computerized Tomography (CT): Among the CT techniques, contrast unenhanced CT is the most accurate to detect and quantify hepatic steatosis [35]. For identifying steatosis, the difference in attenuation of liver and spleen play an important role. In normal liver, the average attenuation value for liver is at least 4 Hounsfield Unit (HU) higher than that for spleen [36]. In contrast, the attenuation value for fatty liver is at least 10 HU lower than that of the spleen [34]. This results in darker appearance of liver rather than brighter. However, CT scans are not sensitive to detect hepatic steatosis less than 30% [37]. Also, studies have shown that unenhanced CT for quantification of macrosteatosis is not clinically acceptable [38]. Moreover, CT uses ionizing radiation to image internal organs which is harmful and is less suitable for follow-up of patients.

4. Magnetic Resonance Imaging (MRI): MRI is non-invasive as well as it does not use any radiation for imaging. MRI can detect hepatic steatosis and is reported to be the most sensitive technique [37,39,40]. MRI can quantify steatosis in terms of Fat Fraction (FF) by acquiring images throughout the liver volume. High accuracy of MRI-FF has been documented by several studies [39,41,42].

MRI for diagnosis of hepatic steatosis

As we aim to simulate MRI signal, this topic provides an insight of what happens when a patient undergoes MRI scanning which helps to figure out minute details (such as magnetic field-spin excess relationship, phase of protons and relaxivity) required for the simulation.

MRI mechanism

Human body comprises of about 70% water by weight. The hydrogen nucleus in water is composed of a single proton which makes it suitable for MRI imaging. The hydrogen has one proton and one electron and both spin around their own axis (Figure 1). Since proton is positively charged and electron is negatively charged, they form a tiny current loop when they spin. This current loop produces magnetic field. However, proton is much larger than electron so the magnetic dipole produced by the proton will dominate over electron.
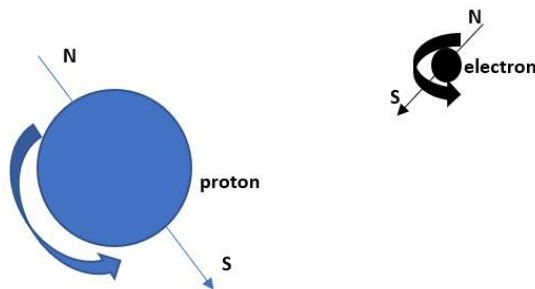
Figure 2-1. Proton and electron spin in Hydrogen atom.

Although the hydrogen atoms possess the property of magnetic dipole, there is no net magnetization in our body because the hydrogen protons are randomly oriented. When an external magnetic field (B_0) is applied to the human body, some of the magnetic dipoles of hydrogen protons align in the direction of B_0 while others align anti-parallel to B_0. At any temperature above absolute zero, at least few of the protons align more in one direction than the other. So, there exists a net magnetization from the protons. The difference in the number of protons in either of the direction is known as 'spin excess'. Although spin excess is small, there are a huge number (Avogadro number) of molecules in each mole of water (i.e. 6.023×10^{23} molecules/mole) and the resulting MRI signal is measurable. After the alignment of protons due to B_0, the spinning protons precess about the axis of B_0 (Figure 2) with frequency ω_0 given by,

$$\omega_0 = \gamma * B_0$$

where, γ is the gyromagnetic ratio which is approximately 42.58 MHz/T for protons.
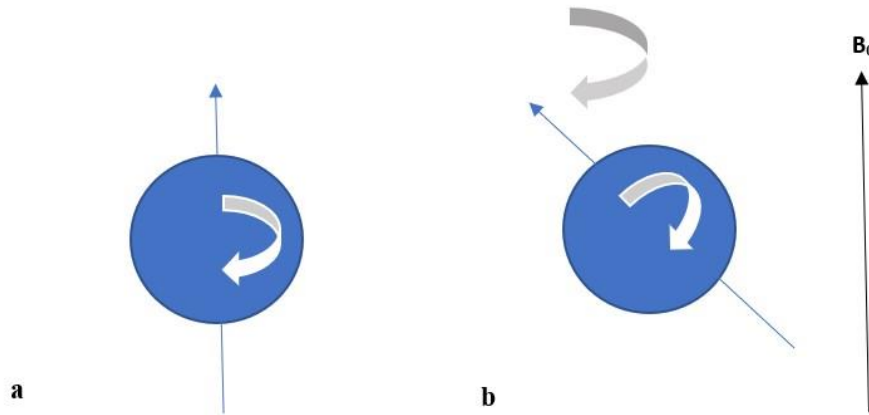
Figure 2-2. Proton spins in the (a) absence and (b) presence of external magnetic field B0
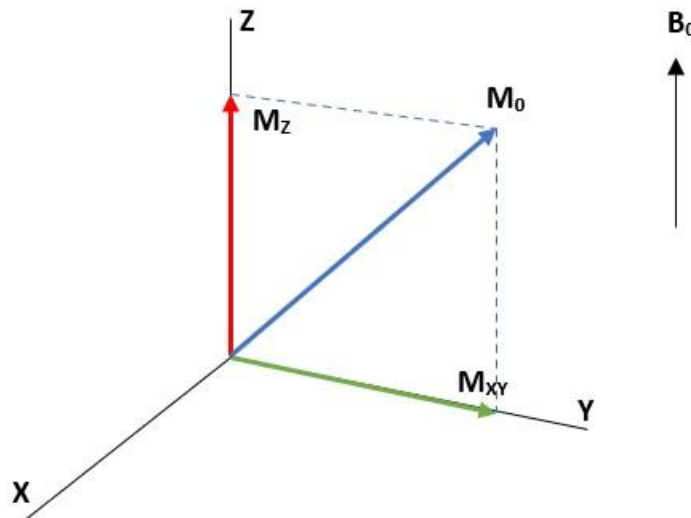
Figure 2-3. Magnetic moment vector of proton

Let M_0 be the magnetization of excess spins that is aligned parallel towards B_0. The components of M_0 (blue arrow) are M_Z (red arrow) and M_{XY} (green arrow) in Z-axis and XY-planes respectively (Figure 3). Even if the number of excess spins is large, the magnitude of M_0 will still be small in comparison to B_0. Hence, to detect signal from the protons, M0 should be tipped onto XY plane (i.e. perpendicular to B_0) which is done by applying a Radio Frequency (RF) pulse whose frequency is same as ω_0 and is oriented in the transverse plane. When the RF pulse is turned off, the M_0 vector starts uncoiling back to its equilibrium position. The phase coherence between all the spinning protons starts to get out of phase.

11

The increase in magnetization in longitudinal direction is caused by the release of absorbed energy from the protons back to the surrounding environment (lattice). This process is known as spin-lattice relaxation and the time taken to restore M_Z is called T1 relaxation, which is represented by,

$$M_Z(t) = M_0(1 - e^{-\frac{t}{T1}})$$

As the magnetization starts to be restored in the Z direction, signal decay occurs in transverse plane due to the dephasing of proton spins with respect to each other. This phenomenon is known as T2 relaxation. Generally, T2 is less than T1 of the order of 5-10 times. The T2 relaxation is given by,

$$M_{XY}(t) = M_{XY}(0) * e^{-\frac{t}{t2}}$$

where, $M_{XY}(0)$ is the initial transverse component of M_0 when it is tipped onto the XY-plane. T2 relaxation is intrinsic and irreversible which occurs by natural interaction among spins. However, the B0 is not uniform which causes magnetic field inhomogeneity and the T2 value decreases further. In this case, T2 is known as T2* which represents the effective transverse relaxation. The T1, T2 and T2* are constant for specific tissue and they are known as relaxation times. The inverse of relaxation times are known as relaxivities (aka, relaxation rates) denoted by R1, R2 and R_2^* respectively.

Fat induced effects in MRI

Hydrogen protons resonate at a constant but unique frequency depending on the molecular structure of compounds. This phenomenon is known as chemical shift which is caused because hydrogen protons experience different magnetic field strength depending upon the chemical environment. The hydrogen protons are provided with intrinsic shielding from surrounding electrons that alters the strength of external magnetic field acting on it. For example, the

hydrogen proton in water (O-H bond) will experience slightly stronger magnetic field as compared to the hydrogen proton in fat (C-H bond) because hydrogen will have less nearby electrons in O-H bond. So, the hydrogen proton in water resonate at a slightly higher frequency. These differences are small and measured in parts per million (ppm) [43]. Due to the difference in resonance frequency, the signals of water and fat will become in-phase and out-of-phase at different time points and introduce oscillations in the MRI signal. Hence, in patients with hepatic steatosis, there arises intensity difference between in-phase and out-of-phase images whereas the intensity of these two images for a normal liver will be same. This principle has been used to detect hepatic steatosis by Dixon [44]. Multiple studies have been conducted using this method describing it as a clinically useful technique to identify and quantify steatosis [45,46]. However, this method is time-consuming, and the images are affected by motion artifacts and magnetic field inhomogeneities and more importantly, Dixon methods do not consider T2* decay and can corrupt fat estimates [47]. This is because for fat quantification, signal is collected over multiple echo times during which T2* decay occurs. Recent studies corrected for the confounding effect of T2* decay by incorporating R_2^* (1000/T2*) into the signal model and simultaneously estimated R_2^* and Fat Fraction (FF) [3,4,48].

Existing issues with signal models

Most of the studies that use R_2^* correction assume the R_2^* decay rate of fat and water to be same (single R_2^*) for simplicity. This technique has been reported to be successful for accurate FF quantification [6,49]. However, if the R_2^* decay rate of fat and water are not similar then single R_2^* model may not be accurate. So, dual R_2^* model which considers independent R_2^* decay rates for fat and water has been proposed and it has been shown that this method improves the accuracy of FF estimation using phantom experiments [50]. However, dual R_2^* is mathematically

complicated and does not perform well with noise which hampers the FF quantification accuracy [51]. Single R_2^* has been demonstrated to be more accurate than dual R_2^* using simulation and phantom studies [51] and patient cohort [52]. There is no common consensus between these two models and current data is limited for which model is accurate to simultaneously quantify FF and R_2^*.

Hence, there is a need to compare the impact of single R_2^* and dual R_2^* correction for estimation of FF. To evaluate the models over entire clinical range of hepatic steatosis, a systematic investigation over a patient population would be necessary but this is not practically feasible. Alternatively, a model-based approach such as Monte Carlo modeling where the simulation of steatosis is done using realistic data from liver biopsy can be useful to reduce or eliminate the need of patient cohorts.

Chapter 3 Automatic Segmentation of Fat Droplets in Hepatic Steatosis using Histology

Introduction

Liver biopsy, the current gold standard to diagnose hepatic steatosis, when imaged under microscope shows FDs as white circular blobs. Analyzing the FF in a biopsy image by a pathologist is time consuming and subjective. So, an accurate and automatic fat quantification method would help to detect NAFLD at an early stage.

Multiple techniques have been used to automate the analysis of quantifying steatosis using liver histological slides [53-57] Some studies used commercial software that quantified steatosis by morphometric analysis. [53,54] More recent studies trained a supervised machine learning model based on annotated images provided by pathologists to identify macrosteatosis regions and calculate its percentage. [55,56] Unsupervised clustering such as k-means has also been implemented for segmentation of FDs. [57] Other approaches used morphological process such as erosion and dilation along with shape features like eccentricity and roundness [58-60]. This study uses thresholding, morphological operation and shape measurements along with a new approach of analyzing the change in area brought by morphological operators to successfully segment the FDs and compute its FF.

Materials and Methods

Sixteen liver biopsy specimens from mice fed for 7 weeks with rich high fat diets were collected. Mice age was 10 weeks and they were all male. The histological slides had 4 μm thick liver tissue with hematoxylin and eosin (H&E) staining. An inverted fluorescence microscope (Nikon Eclipse), equipped with a digital camera was used to capture images. The images were acquired at 4X, 10X and 20X-magnification using *Bioquant Osteo* software. The total size of an image was 1280X960 pixels. The images were captured such that they cover complete liver

sample under observation. The slide was placed on the stage of the microscope and the stage was shifted first horizontally and then vertically to capture all the regions of the sample. While moving the stage, special attention was provided to the X and Y coordinates of the corner edges of the previous position.
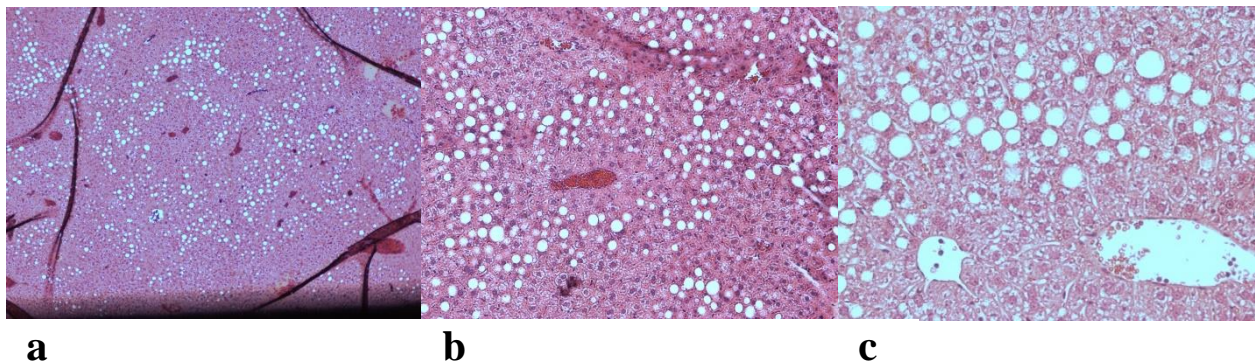
Figure 3-1. Liver histology images with different magnifications: (a) 4X, (b) 10X and (c) 20X for a mice-fed with a high-fat diet.

Generally, lipid droplets appear as white circular blobs with sharp edges on digital images but all the pixels might not be completely white; some being pink in color (similar to background due to staining) while other being grey (due to reflection, refraction or inadequate light of microscope while imaging). In addition, there are other structures that are circular or appear white such as sinusoids, portal veins, centrilobular veins or tissue cracks. Different structures present in liver biopsy images that can confound the segmentation of FDs are shown in figure 2. These other structures need to be discarded while segmenting the FDs. Moreover, the close-by FDs can sometimes attach with each other and lose their circular shape as shown in Figure 2. A pseudo code to segment FDs is presented in Figure 3.
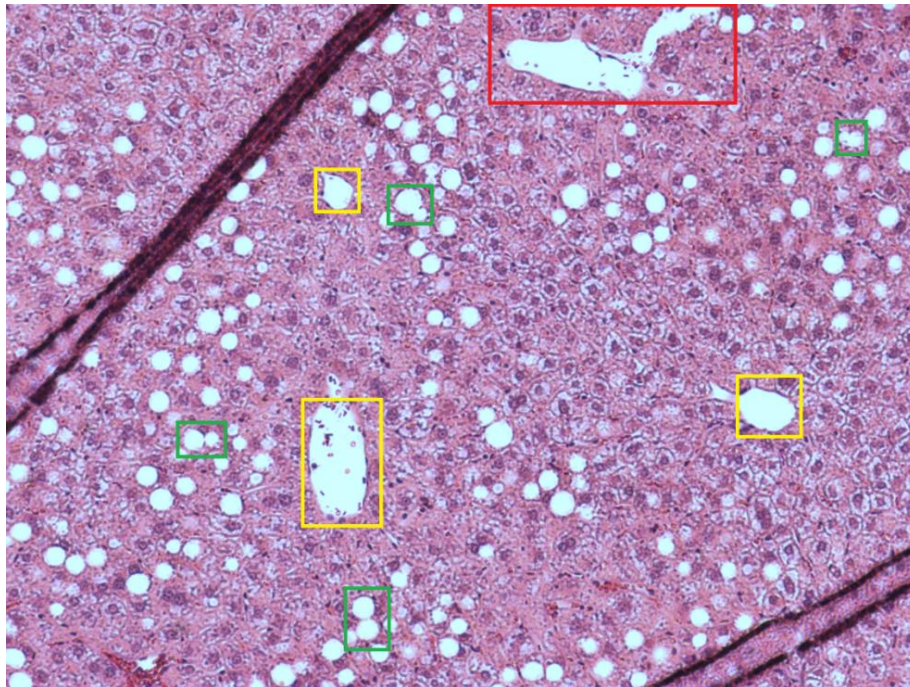
Figure 3-2. Image at 10x magnification showing different regions in liver histology. The yellow boxes are non-fat white regions. The green boxes show attached FDs that do not appear circular. The red box represents large white region which cannot be discarded by thresholding and size constraint is imposed for not considering it during segmentation.

Thresholding and small objects removal

As the fat vacuoles appear white, they have high intensity value and can be segmented out from other regions by using thresholding. The images had different brightness conditions so manually picking a value did not work. Otsu's method [61] which works by minimizing the intra-class variance of black and white pixels, was implemented (function threshold_otsu() in Figure 3) to automatically fix the threshold based on the characteristics of the image using *skimage* library in Python (Python Software Foundation). The tiny circular white droplets, which occur as a residual of thresholding operation could be falsely considered as lipid droplets and were discarded by removing objects smaller than a threshold value (function small_objects_removed() in Figure 3).

FD_Segmentation()

$MIN\_OBJECT\_SIZE, MAX\_DISK\_SIZE \leftarrow threshold\_val\_depending\_on\_magnification$
$disk\_size \leftarrow 2$
$selected\_objects \leftarrow list()$
$img \leftarrow read\_image()$
$grayscale \leftarrow convert\_grayscale(img)$
$thres \leftarrow threshold\_otsu(grayscale)$
$thres\_img \leftarrow grayscale > thres$
$smo\_removed \leftarrow small\_objects\_removed(thres\_img, MIN\_OBJECT\_SIZE)$

for $obj \leftarrow smo\_removed$ **do**
  if round(obj) **then**
    $selected\_objects \leftarrow append(obj)$
  end if
end for

while $disk\_size \leq MAX\_DISK\_SIZE$ **do**
  $erode \leftarrow morphological\_erosion(smo\_removed, disk\_size)$
  $dilate \leftarrow morphological\_dilation(erode, disk\_size - 1)$
  for $obj \leftarrow dilate$ **do**
    if round(obj) **then**
      $selected\_objects \leftarrow append(obj)$
    else
      if seperate_joint_objs_check_roundness(obj) **then**
        $selected\_objects \leftarrow append(obj)$
      end if
    end if
  end for
  $disk\_size \leftarrow disk\_size + 1$
end while

Figure 3-3. Pseudocode for segmentation of FD

Morphological Operation

The images were then processed using morphological erosion and dilation operation (function morphological_erosion() and morphological_dilation() in Figure 3). The operation was applied iteratively until all the droplets were segmented. In each iteration following values were modified:

1. Structure disk size was increased.

2. Minimum object size to be discarded and maximum object size to be considered was reduced.

3. The maximum eccentricity value was decreased, and the minimum roundness value was increased.

To extract FDs that coalesce into single blobs and does not appear circular, morphological operation with structure size=n-1 for dilation and structure size=n for erosion was used as shown by dilate <- morphological_dilation(erode, disk_size-1) in pseudocode (Figure 3). Later while segmenting FDs, the eroded image was dilated with structure size=n.

Segmenting Lipid Droplets

After each iteration of morphological operation, all the regions were checked against their eccentricity, roundness value and area change after morphological operation. Eccentricity shows how uncircular an object is, so region with eccentricity value less than a threshold value (t_e) was preferred while objects with roundness value greater than a specific value (t_r) was chosen. The t_e and t_r depended upon the magnification of image. With later iterations, structure disk size for morphological operation increased. The higher disk size can produce circular objects from non-circular ones by removing long elongated portion of it. To account for this, its change in area after the operation was computed and it was rejected if the change was higher than expected (differed with magnification of image). All of these details has been represented abstractly by round() function in the pseudocode (Figure 3). Finally, the regions that passed all these tests were considered as FDs. In the pseudocode shown in Figure 3, the selected_objects list represents a list of objects/regions selected as FDs.

Results

By using the thresholding and morphological operation to the H&E stained liver histology images, segmented image along with the number of FDs and FF were obtained in an automated manner. Otsu's method for thresholding was tested on grayscale image as well as red, green and blue channels individually and was found that thresholding worked better on grayscale images. The results obtained from the automated segmentation indicated that FF of the mice liver specimens ranged from 0.05 to 11.5% with a mean of 5.37±2.79%. The segmented images were verified qualitatively by pathologist but in the absence of ground truth segmentation result no numeric value for the accuracy of the segmentation could be computed.

Figure 4 shows the segmentation result for 4X, 10X and 20X images. The 4X images provided wide field of view but the FDs were tiny and difficult to be picked by the segmentation algorithm as shown in Figure 4a where there are unpicked FDs. In contrary, for 20X images the FDs were big, and a clear boundary of FD helped to improve the accuracy of algorithm (Figure 4c). The 10X images had a balance of area coverage and FD details as demonstrated by Figure 4b.

a
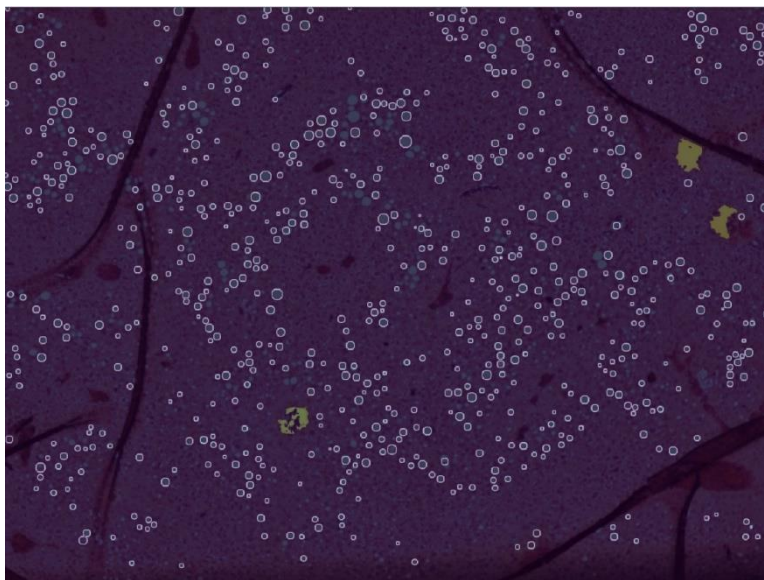
b
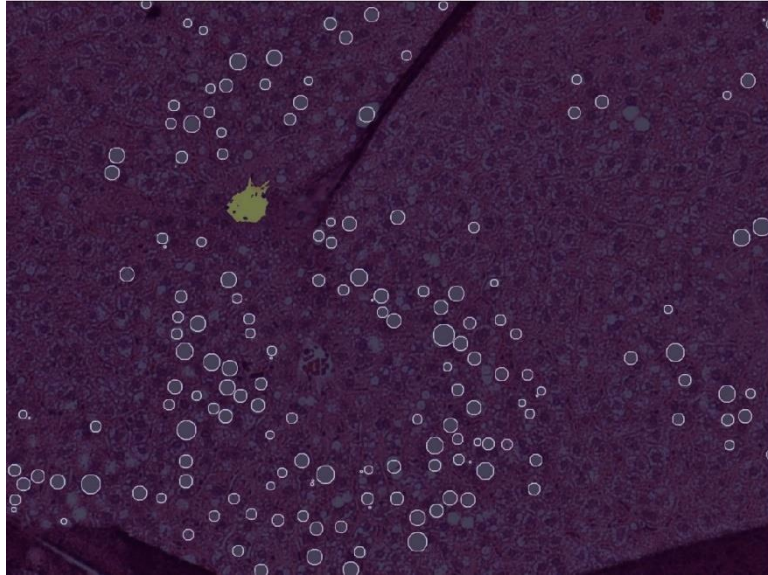
c
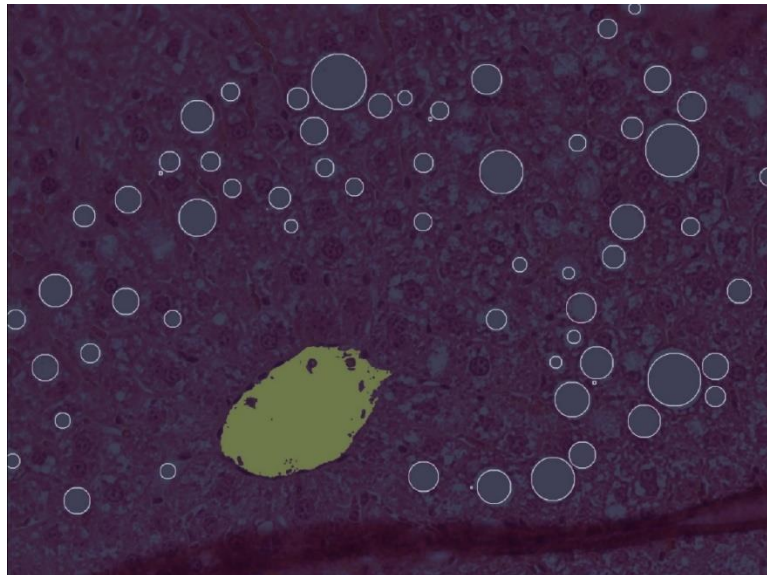
Figure 3-4. Segmented Images. The yellow region represents the discarded region and grey circular objects represent FDs. (a) 4X with 699 FDs and 5.74% FF. (b) 10X with 167 FDs and 4.87% FF. (c) 20X with 66 FDs and 8.78% FF.

Discussion and Limitations

Quantification of hepatic steatosis is a difficult task. Our visual system is well suited in analyzing structure and distinguishing them but designing computerized technique to do so is challenging. Our technique was able to segment FDs with qualitative validation from pathologist.

In our method, thresholding played an important preliminary role by eliminating the background pixels as well as disjoining close FDs. Morphological operation polished the process by enabling the detection of coalesced FDs that were weakly connected. When the disk size was increased, its degree of disconnection increased and it separated FDs that were joined along a larger arc that led to the loss of their circularity and hence, allowed choosing them as separate fat bubbles. However, this process could produce circular structure from elongated sinusoids or tissue cracks. This was partially resolved by analyzing the area change after the operation.

The implementation was able to exclude larger white regions as well as white circular non-fat objects. It also succeeded in capturing the joint FDs that do not appear as circle. To separate connected lipid vacuoles, different structure size for opening and dilation was used. This well suited the purpose, but it generated minor deviations from original size of the droplets. The combination of roundness and eccentricity increased true positive. Sinusoids that are U-shaped can have less eccentricity, but they get rejected by the roundness threshold.

Proper analysis of the segmentation of FDs can be useful to understand the pattern and characteristics of them which will help to estimate the morphology of lipid droplets in different pathologies.

There are some limitations in this study. Firstly, the maximum FF that could be obtained from the liver samples were less than 15% which is not sufficient to cover the entire clinical range of hepatic steatosis. Secondly, this segmentation method needs to be tested with higher FFs. In addition, this segmentation technique was not cross validated with more rigorous manual segmentation by pathologists such as manual point counting.

Chapter 4 Characterization of Hepatic Steatosis – Gamma Distribution Function

Introduction

Several studies have been conducted to study the properties of FDs with an objective to detect FDs and quantify FF as well as number of FDs in liver. Characteristics of FDs is important to mimic realistic hepatic steatosis that can serve as an alternative technique to analyze MRI relaxivity. However, as per our knowledge, no study has used the properties of FDs to simulate hepatic steatosis. Some studies have analyzed the circular morphology and smooth edge contour of fat globules [57] while others have compared the shape of clustered and separate FDs with other empty spaces [62] to identify FDs. Moreover, area and diameter of FDs has previously been quantified to distinguish them from other white regions [53] Also, a strategy to lay a square tile over liver biopsy image has been previously implemented to evaluate the regional inflammation accumulation [63]

Prior work has been successful to quantify FF with high accuracy and distinguish different structures present in liver [53,57,62]. They have analyzed the shape and eccentricity of FDs and classified them based on their organization. However, they have mostly been qualitative analysis because of limited number of clinical specimens. Hence, the objective of this research was to quantify the size of FDs and position of FDs with respect to each other and perform statistical modeling of those quantities to build a virtual model of hepatic steatosis mimicking true histology that can serve as an alternative platform for further experiments related to steatosis.

Materials and Methods

Histological analysis

The segmented images in Chapter 2 were used to analyze the morphology and clustering behavior of FDs by calculating their radius, inter-particle distance and inter-regional variation

(regional anisotropy) in a liver specimen. The "skimage" library's *measure.regionprops* function was used to get those values. The pixels whose value differs by ~1 and are connected are considered as a single region by the function. It provides the minor axis as well as the major axis of the region; the length of the minor axis was considered as the radius of the region.

To estimate the inter-particle distance, nearest neighbor (NN) distance was considered. The NN distance shows how the droplets are present with respect to each other that indicates the separation between them as well as their tendency to arrange in group. In actual liver, FDs are distributed by 3D NN distance but as we had 2D images of liver biopsy 2D NN distance was computed by first tracking the centroids of each FDs, then calculating the distance between the centroid of each FD with that of other FDs and finally evaluating the shortest distance between them.

For analyzing the accumulation of FDs within certain region (regional anisotropy), 120 μm side square grid, roughly six times the mean hepatocyte dimension, was laid over the segmented image. Then the amount of FF within each region was calculated and normalized to the maximum value for each image, i.e. the scale of histogram in X direction was set in the range [0, 1].

Statistical Description

To examine the relationship between FF and the characteristics of the FDs, a generalized Gamma Distribution Function (GDF) was selected because it is flexible such that Chi-square, exponential, Erlang and Weibull distributions are special case of it, obtained by different combination of the parameters. A GDF has two parameters: shape (γ) and scale (β). Generally, the γ parameter defines the height of the distribution and β parameter is related to its width (Figure 1). The GDF can be expressed as,

$$GDF(x) = \frac{1}{\beta * \Gamma(\gamma)} * \left(\left(\frac{x-\mu}{\beta}\right)^{\gamma-1} * \exp\left(\frac{x-\mu}{\beta}\right)\right) \qquad (1)$$

where, μ is the location parameter. $\beta > 0$, $\gamma > 0$, $x \in [0;\infty)$, $x \geq \mu$ and $\Gamma(\gamma)$ is the Gamma function evaluated at γ given by,

$$\Gamma(\gamma) = \int_0^\infty t^{\gamma-1} e^{-t} dt \qquad (2)$$

The gamma function in Eq. 2 is generally used as an extension of the factorial function to real and complex numbers. The GDF in Eq. 1 was used to model the properties (radius, NN distance and regional anisotropy) of lipid droplets at different fat concentrations. For this purpose, the location parameter μ was considered to be 0, i.e., standard gamma distribution.
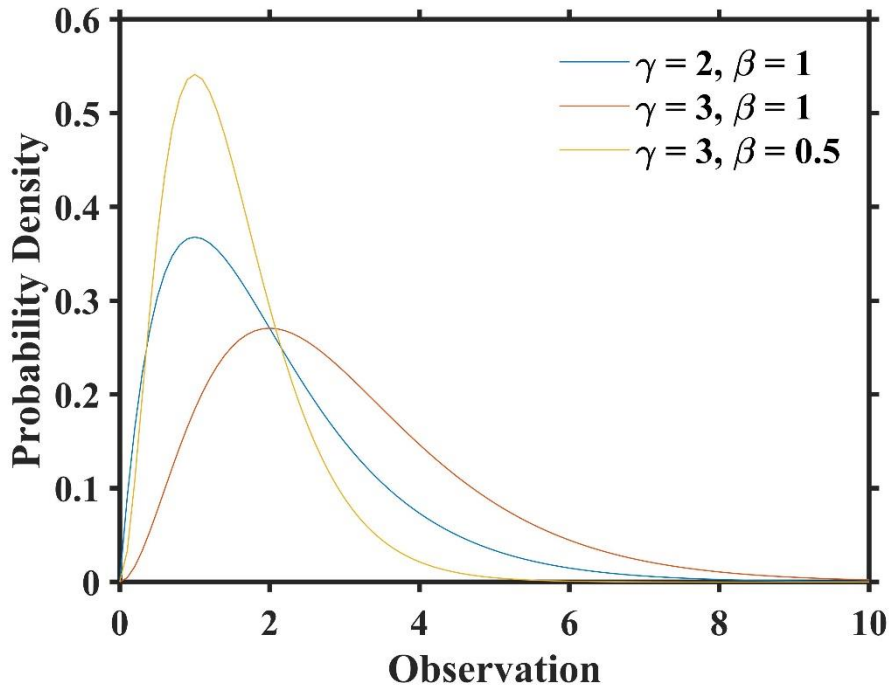
Figure 4-1. Gamma Distribution Function (GDF) with different shape and scale parameter

After representing each properties of FDs with their respective GDF, the gamma parameters of each distribution were generalized with respect to FFs using regression analysis.

25

Model Generation

To simulate a liver volume, a cuboid of 600X600X120 μm^3 dimension was designed. The fat

vacuoles were placed as a spherical impenetrable ball in the simulated environment until the

desired FF was reached. No other anatomical structures such as sinusoids were considered for

the simulation. To generate a sphere, its size was estimated from lipid droplet size histograms.

The spheres were distributed in two different ways:

1. Random Distribution

Pseudocode to simulate random distribution of FDs is shown in Figure2. The generated fat

spheres were placed in the virtual environment using Gaussian random distribution. They were

not allowed to overlap with each other and if a collision was detected (function collision() in

figure 2) then the FD was placed on the boundary of the colliding FD (function

surface_colliding_fd() in figure 2) and the collision test was repeated until the collision was

resolved or a specified number of attempts were made. A new random position for the FD was

generated (function random_location() in figure 2) if the collision was still present after the

specified attempts and the process was repeated.

2. Distribution based on regional anisotropy with NN distance

The virtual environment was like (a), but the FDs were placed according to the GDF of the

NN distance with respect to each other within the 120 μm region. The FF in each region 120 μm

was determined using the GDF of the regional anisotropy. First FD was placed randomly then

every next FD was placed at NN distance, provided by the inter-particle histogram, from the

previous FD. Collision was checked like (a) with additional resolving measures. If collision

could not be resolved within specified attempts, then a new NN distance was generated, and the

sphere was placed without changing the reference sphere. If the collision still existed after

certain iterations, then a new reference sphere was chosen, and the process was repeated. Finally, to avoid infinite attempts, if collision was still present then the sphere was positioned in a new random location.

The simulation model was shown as a three-dimensional liver volume using the best GDF parameters. To validate the distribution of FDs using the model, virtual 4 μm thick 2D cross-sections were visually compared with the corresponding true histology tissue images.

```
Random_Simulation(x_lim, y_lim, z_lim, ff)

cur_fat_vol ← 0
MAX_SAME_FD ← 500
MAX_ATTEMPT ← 100
req_fat_vol ← ff * x_lim * y_lim * z_lim

while TRUE do
    r ← GDF(γ_radius, β_radius)
    x, y, z ← random_location(x_lim, y_lim, z_lim, r)
    fat_vol ← 4/3 * π * r³
    if fat_vol + cur_fat_vol ≤ req_fat_vol then
        same_fd ← 0
        attempts ← 0
        flag ← FALSE
        while same_fd ≤ MAX_SAME_FD do
            if collision(x, y, z, r) then
                x, y, z ← Surface_colliding_fd(r)
                same_fd ← same_fd + 1
            else
                loc ← append(x, y, z)
                radius ← append(r)
                cur_fat_vol ← cur_fat_vol + fat_vol
                flag ← TRUE
                break
            end if
        end while
        if not flag then
            while attempts ≤ MAX_ATTEMPT do
                x, y, z ← random_location(x_lim, y_lim, z_lim, r)
                if collision(x, y, z, r then
                    attempts ← attempts + 1
                else
                    loc ← append(x, y, z)
                    radius ← append(r)
                    cur_fat_vol ← cur_fat_vol + fat_vol
                    flag ← TRUE
                    break
                end if
            end while
        end if
        if not flag then
            break
        end if
    else
        break
    end if
end while
```

Figure 4-2. Pseudocode to simulate hepatic steatosis using random distribution of FDs

Results

Microscopy Analysis

The size and distribution of lipid droplets were examined from sixteen segmented images. Figure 3(a) is an image collected from the microscope at 10X of a liver biopsy specimen with FF 9.48%. The magnification helped to capture the variations in FDs. Figure 3(b) shows regions in original image selected as FDs. The images were segmented as described in Chapter 2 using thresholding and iterative morphological operation. The information extracted from these images are listed below.

a
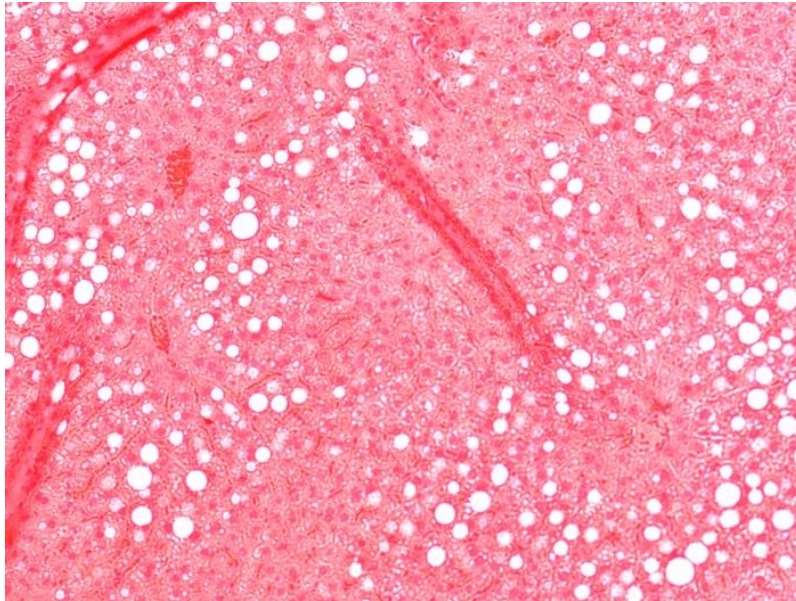
b
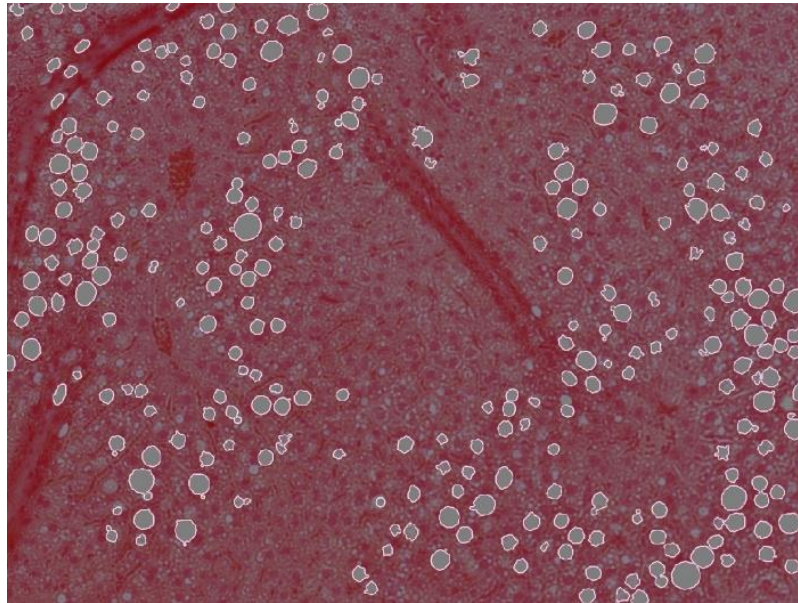
Figure 4-3. Histology image collected from the microscope at 10X magnification of a liver biopsy specimen with FF of 9.48% (a), and segmentation mask of FDs laid over the original image (b). The FDs are depicted as white circular objects

(a) Cellular lipid droplets size distribution

The radii of the lipid droplets for different FFs were extracted from the segmented masks and their histogram was plotted with the fitting of corresponding GDF. Figure 4a represents the histogram for three representative liver samples with different FFs. As FF increases the peak of the histogram moves towards right indicating increase in number of FDs with larger size.

The shape (γ) and scale (β) parameter of GDF were fitted by doing regression analysis with respect to FF. β showed a linear trend and moderate correlation with FF, $\beta = 0.0809*FF+0.3188$ ($R^2 = 0.490$) as shown in Figure 4b. The γ parameter showed a strong linear relationship with the β parameter of GDF, allowing to accurately estimate its value using the equation $\gamma = -13.254*\beta+23.144$ ($R^2=0.819$), which is shown in Figure 4c.

a

b

$\beta = 0.0809*FF + 0.3188$
$R^2 = 0.490$

c

$$\gamma = -13.254 \cdot \beta + 23.144$$
$$R^2 = 0.819$$
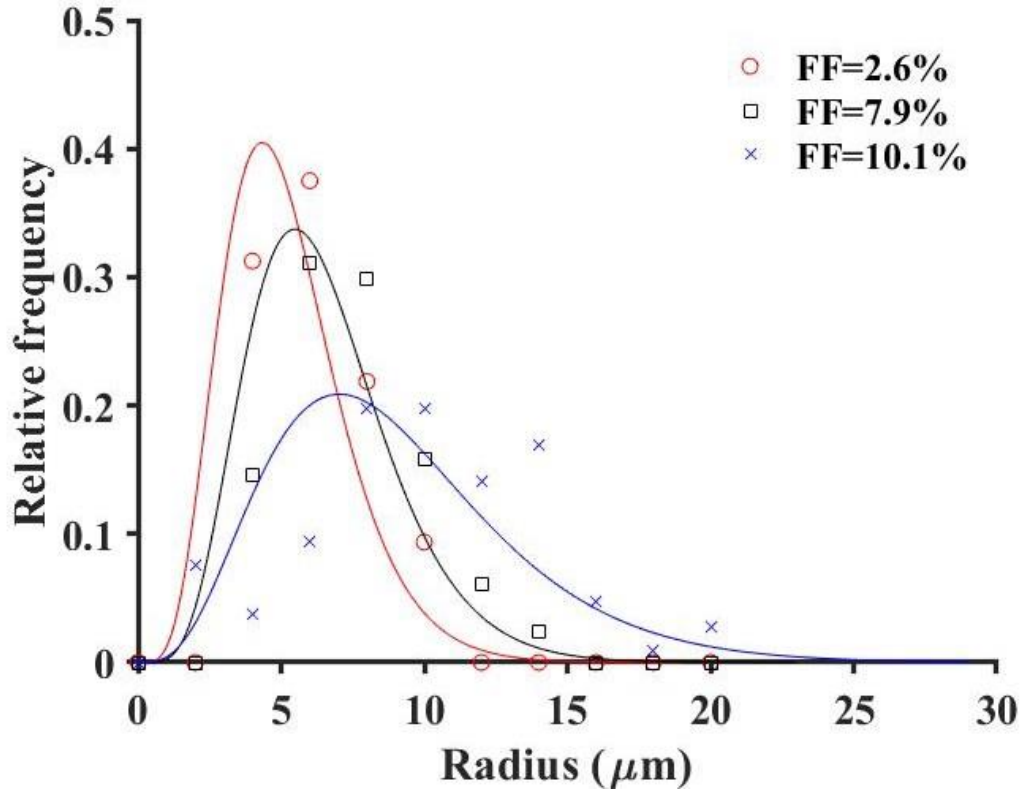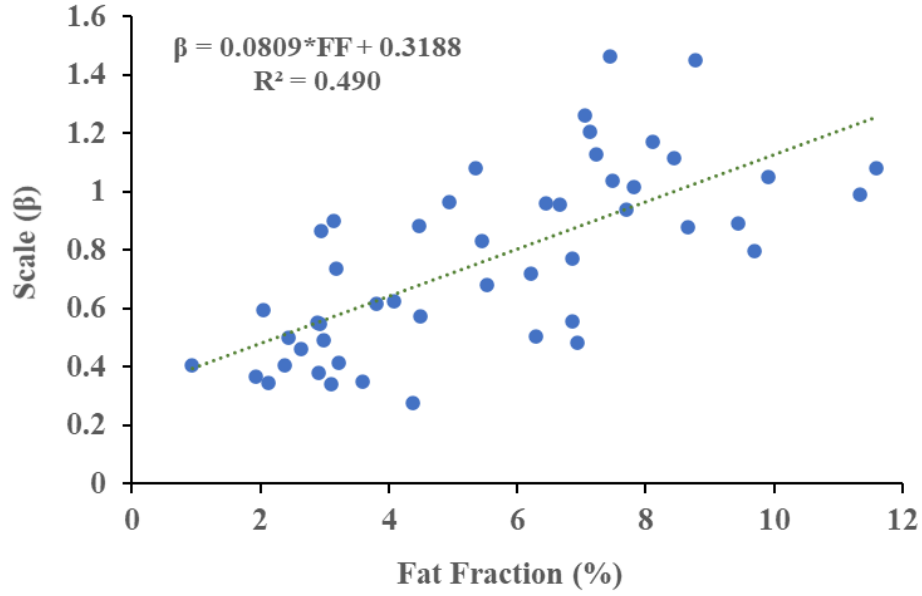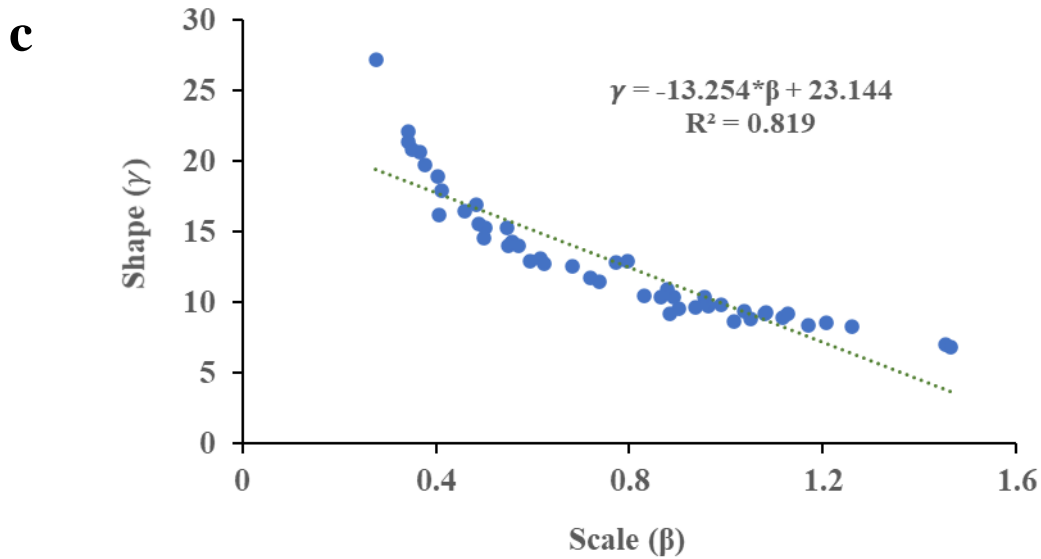
Figure 4-4. Lipid droplet size distribution: (a) The graph demonstrates the relative frequency of lipid droplets as a function of their radii for three different FFs of liver sample. It shows that the size gets bigger with increase in FF. Linear regression plots show the relationships between β and FF (b) and γ and β (c).

(b) Inter-particle distance

NN distance was calculated as shown by yellow lines in Figure 5a. After analyzing the distance between all FDs, the shortest distance was chosen. The NN distances between the FDs were calculated and their histogram was plotted as shown in Figure 5b. The plot shows that as the FF increases the FDs are more tightly packed. Figure 5c demonstrates that the β parameter of the NN GDF is moderately corelated to the FF ($R^2 = 0.5241$) for linear regression and is represented by $\beta = -0.7777 \cdot FF + 10.259$. The γ parameter had a similar linear relationship with FF, given by $\gamma = 0.7535 \cdot FF + 3.8343$ ($R^2 = 0.4845$) as shown in Figure 5d. However, it had comparatively strong relationship ($R^2 = 0.7254$) with β parameter of the GDF, shown by Figure 5e, which enabled more accurate computation using the relationship $\gamma = -0.8583 \cdot \beta + 13.116$.

a

b

c

$$\beta = -0.7777*FF + 10.259$$
$$R^2 = 0.5241$$

Scale (β) vs Fat Fraction (%)

d

$$\gamma = 0.7535*FF + 3.8343$$
$$R^2 = 0.4845$$

Shape (γ) vs Fat Fraction (%)

e

$\gamma = -0.8583*\beta + 13.116$
$R^2 = 0.7254$
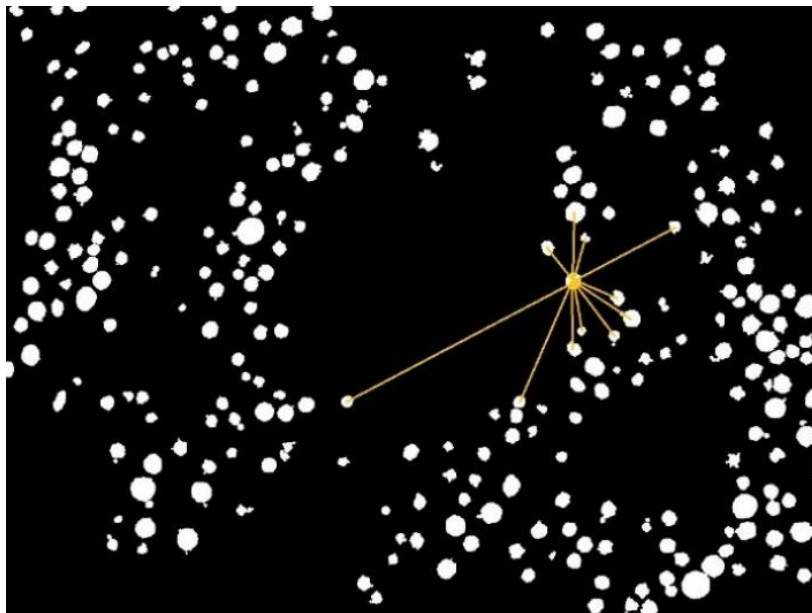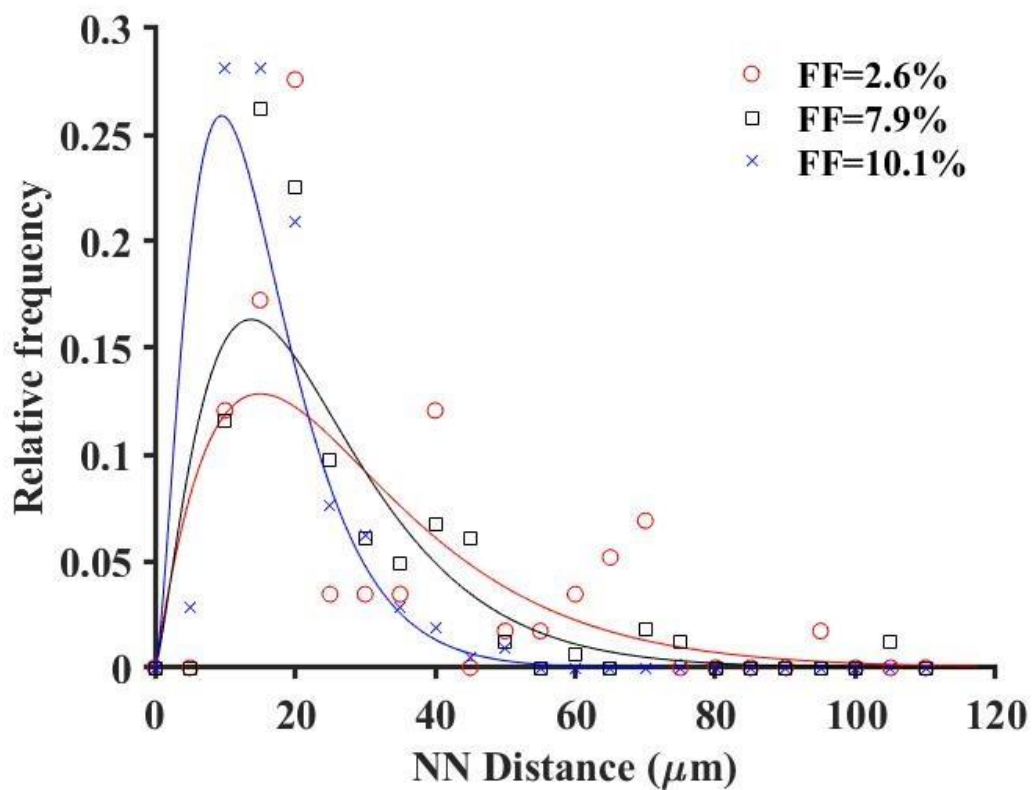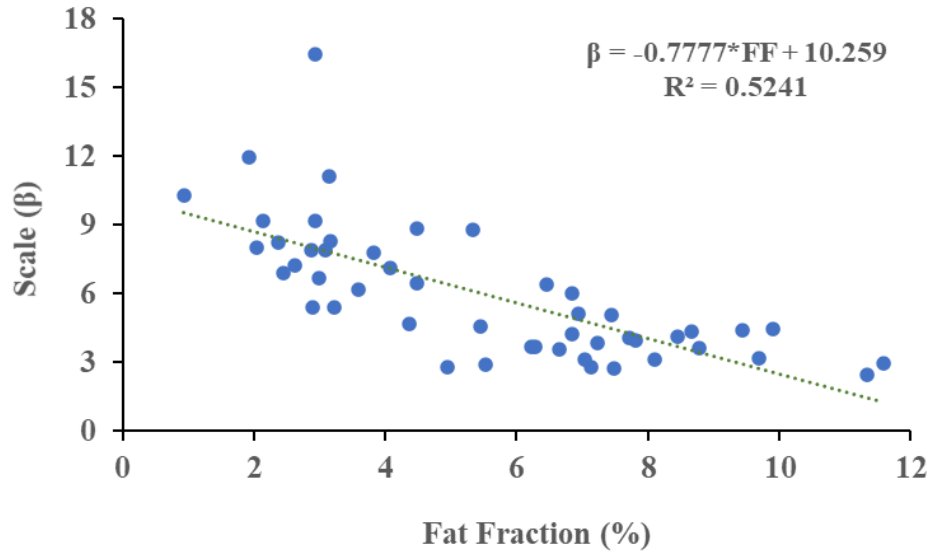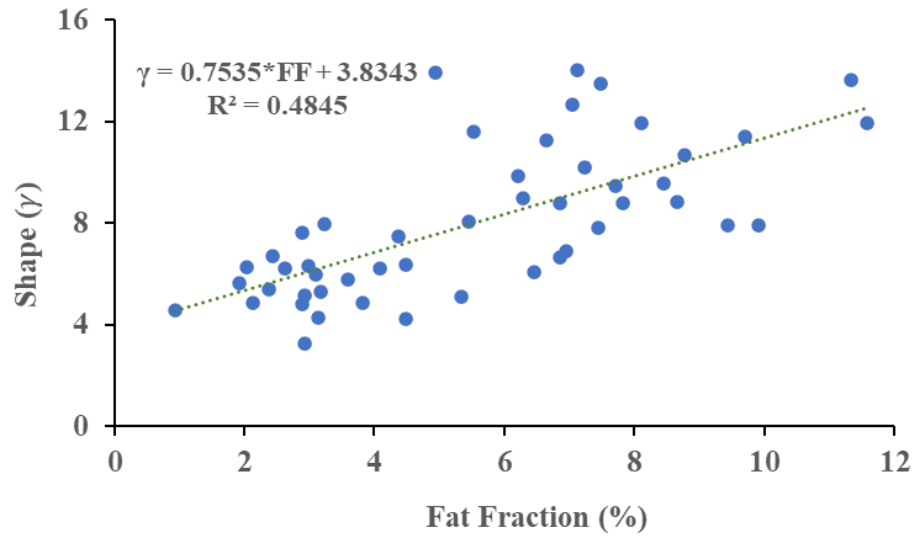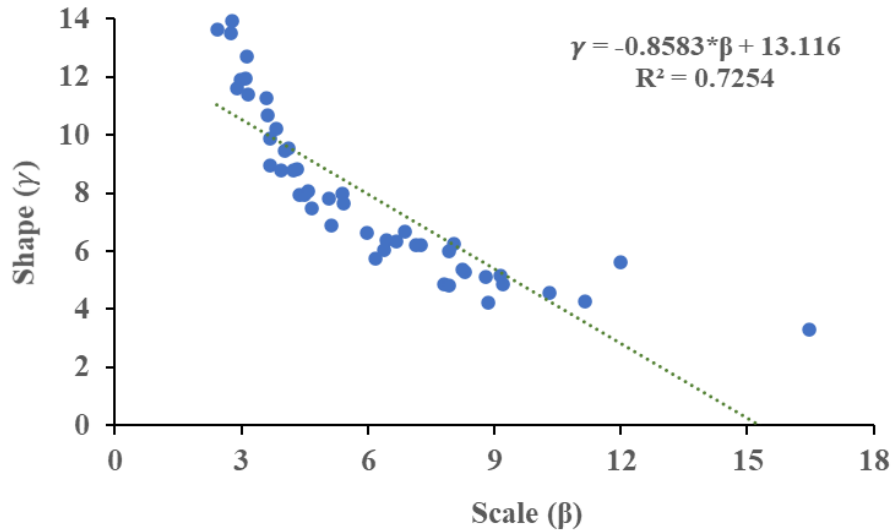
Figure 4-5. Inter-particle distance: (a) Image showing NN distance estimation between FDs after automatic segmentation. (b) The graph demonstrates the NN distance histogram for three different FFs of liver specimens. It indicates that as the FF increases the distance between FDs decreases. (c) The plot shows the relationship between β and FF. (d) The graph shows how γ is correlated with FF. (e) The plot shows how γ varied with β.

(c) Regional Anisotropy

Regional anisotropy is the difference in deposition of FDs among regions in liver biopsy image. For regional anisotropy, the distribution followed an exponential curve for low FF due to the absence of fat deposition in most of the regions. With increase in FF, the distribution shifts towards right showing more regions with higher FF (Figure 6a). The β parameter is weakly correlated to the FF ($R^2 = 0.27$) showing a linear relationship represented by $\beta = 0.009 * FF - 0.0049$ (Figure 6b). The γ parameter demonstrated a moderately correlated exponential relationship ($R^2 = 0.56$) with the β parameter of the GDF given by $\gamma = 3.5949 * e^{-18.98*\beta}$ (Figure 6c).

34

a

b

$\beta = 0.009*FF - 0.0049$
$R^2 = 0.272$

c

$\gamma = 3.5949e{-}18.98{*}\beta$
$R^2 = 0.556$
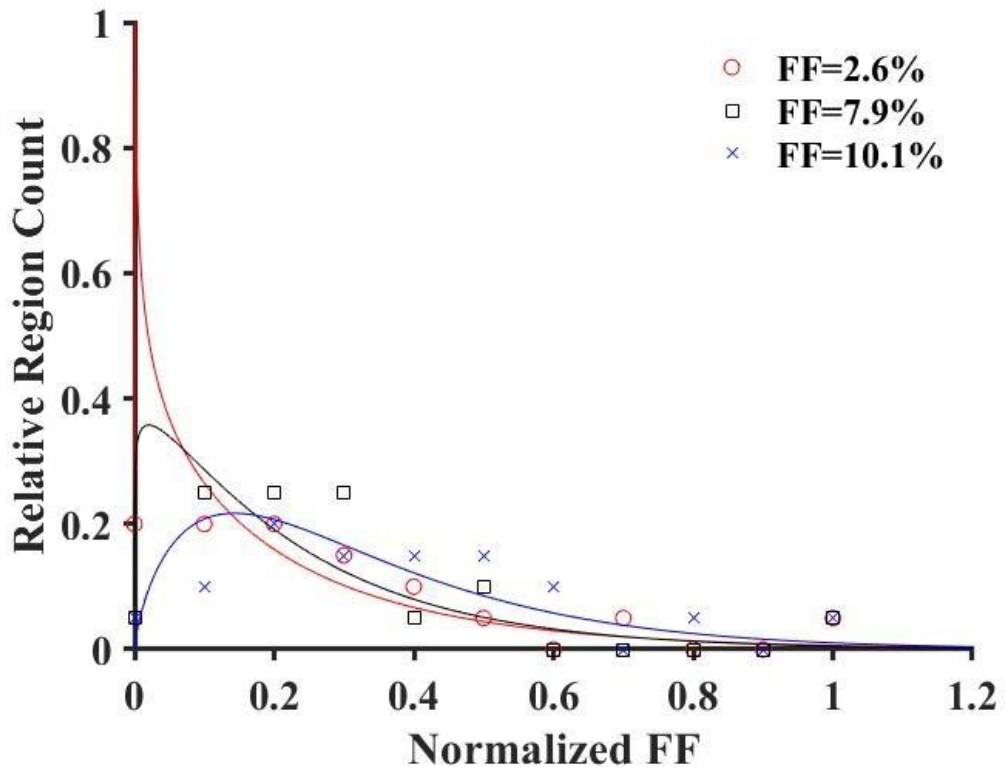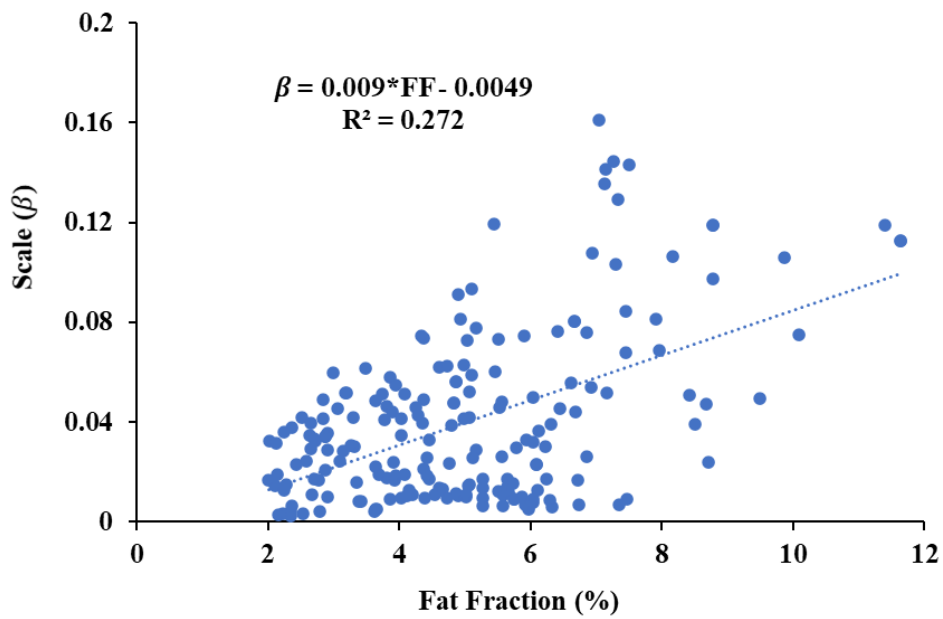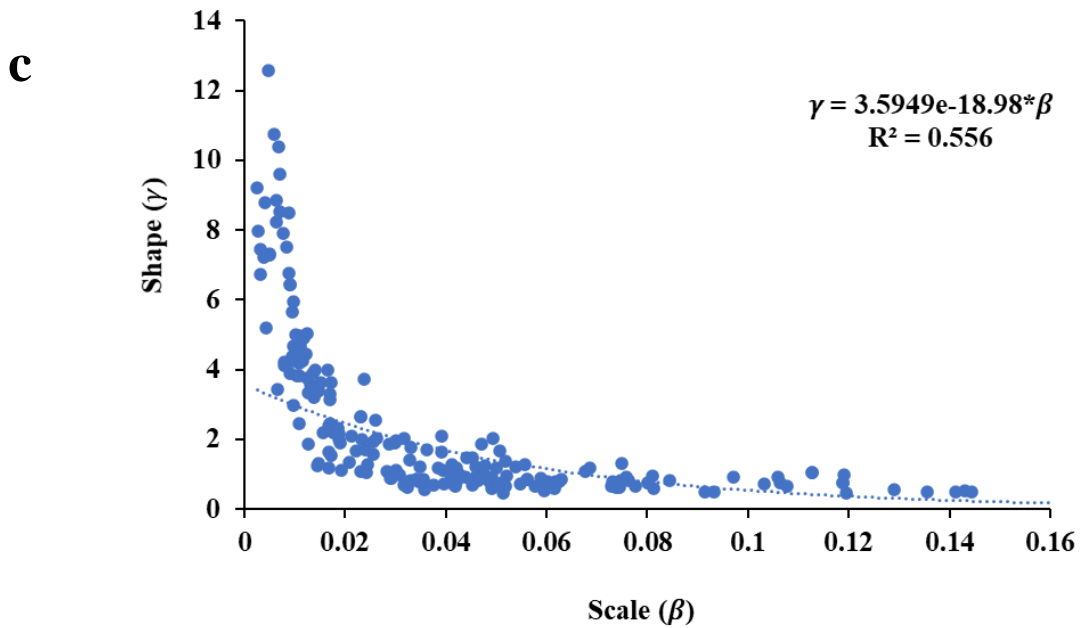
Figure 4-6. Regional Anisotropy. (a) The graph demonstrates the regional anisotropy histogram for three representative FFs of liver specimens. It indicates that as the FF increases the number of regions with the absence of fat deposition decreases. (b) The plot shows the relationship between β and FF. (c) The graph shows how γ is correlated with β.

Simulated Liver Model

A comparison of model generated fat morphology and actual histological sample using two different distributions of FDs for FF of 8% is shown in Figure 7. The 3D cuboid represents a 600X600X120 simulated liver geometry with FDs shown as white spheres (Figure 7a and 7b). A random 4μm thick cross-sectional view of the corresponding volume is represented in Figure 7c and Figure 7d along with histology specimen in Figure 7e. Random Distribution of FDs does not show realistic accumulation of FDs. Implementation of nearest neighbor statistics helps to mimic the grouping characteristic of FDs and regional anisotropy distributes the accumulated FDs among different regions. Note that all the regions of predicted morphology for regional

anisotropy with NN does not have equal volume of FDs and demonstrate in-vivo clustering behavior of FDs.
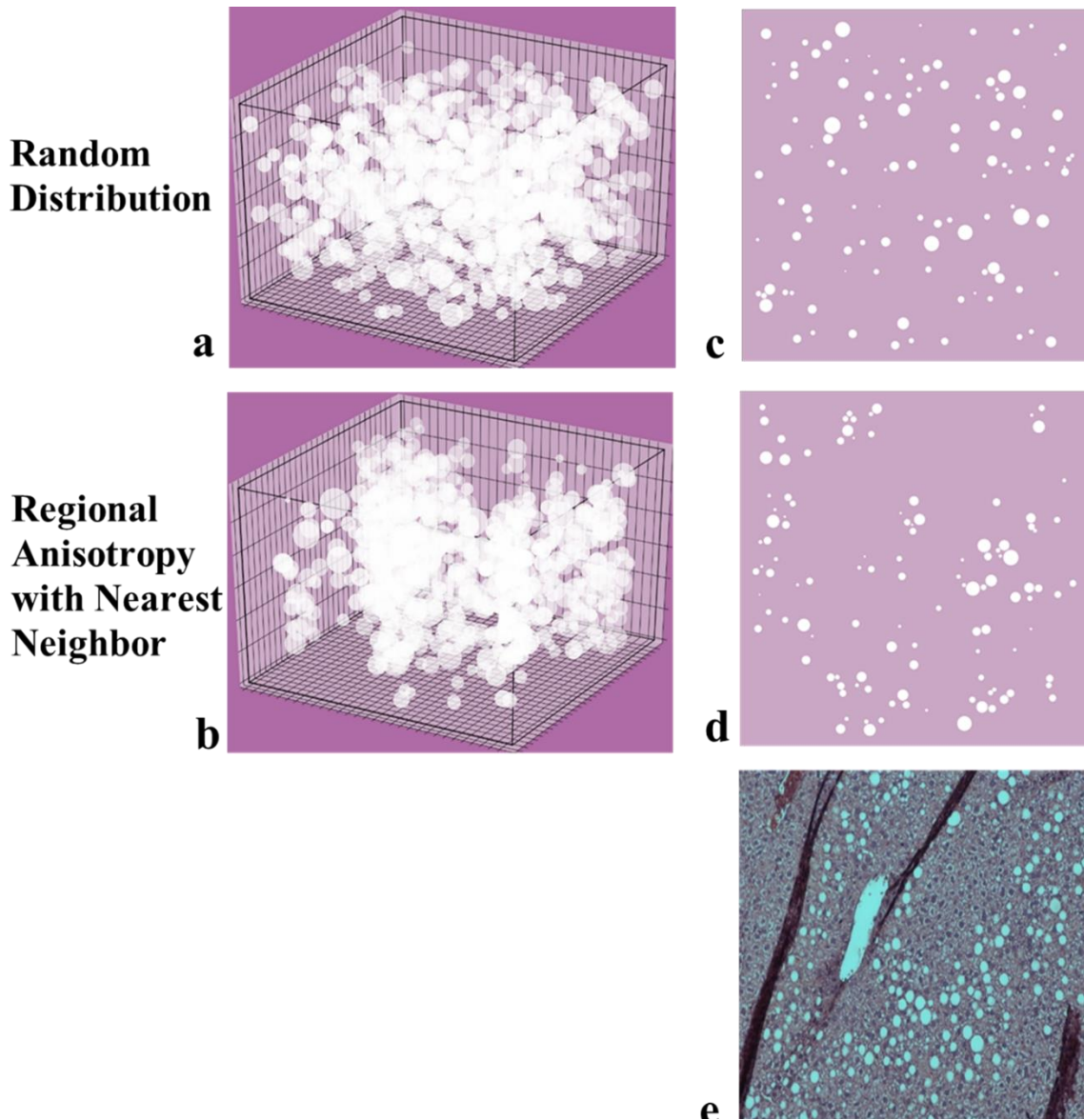
Figure 4-7. Model predicted fat morphology with 8% FF in a 600X600X120 liver volume. Random (a) and regional anisotropy with nearest neighbor (b) distribution of FDs (depicted as white spheres) in 3D liver geometry and corresponding 4μm thick random sections of the 3D models (c, d), and actual histological section with 8.16% FF (e). Note the similarity between (d) and (e). The FDs in (e) are seen around a large white vacuole. Similar clustering behavior is shown by FDs in top left quarter of (d) (large white vacuole not shown).

Discussion and Limitations

The main aim of this study was to create a statistical model to describe the size and morphology of FDs in tissue. Accurate simulation of morphology of FDs will help to mimic synthetic MRI signals in the presence of fat and analyze the R_2^* decay curves for different FFs. In this research, the method of statistical modeling was experimented with low FF and data from mice with hepatic steatosis. But this technique can be generalized to higher FF and be applied to other diseases associated with fat accumulation such as fibrosis and cirrhosis.

The size, inter-particle distance and inter-region variation of FDs could be well characterized by GDF but it failed while modeling regional anisotropy for FF less than 5%. It is because of low FF that most of the FDs were accumulated in certain regions of liver sample leaving large portions of it with no fat. This caused the distribution data to be mostly zero. The GDF for low FFs using 120X120 square grid showed that almost 65% of the region had no fat accumulation. It also demonstrated that such region is decreasing with increase in FF which is a positive sign that regions with no FF are encountered less at higher FFs. This suggests that more robust relation between regional anisotropy and FF can be generated with wide FF range.

This work assumes 2D distance between FDs for measuring inter-particle distance but in reality, the FDs are in 3D space and for more accurate estimation of NN distance, 3D environment should be considered. Nevertheless, this approach successfully simulated hepatic steatosis to any given FF within the range 0%-13% that showed resemblance to actual histology. The range of simulation is limited by the regression equations estimated for size and NN analysis at only low FFs. We believe that the simulation can be expanded to create steatosis models with wide clinical FF ranges by performing this experiment with variety of samples including low to high FFs.

Chapter 5 Relaxivity-Fat Calibration in Hepatic Steatosis: Design of a Monte Carlo Model

Introduction

Recent development in MRI has increased its clinical acceptance as a non-invasive technique to assess hepatic steatosis. Further, single and dual R_2^* MRI models have been proposed for quantification of FF but there is no common consensus between these two models and current data is limited for which model is accurate to quantify FF.

To understand the relationship between relaxivity and FF and determine a signal model for accurate estimation of FF and R_2^*, we use a computational procedure to produce a realistic liver volume with hepatic steatosis. The liver geometry was used to mimic desired FF (as discussed in Chapter 4) and MRI signal is simulated at field strengths of 1.5T and 3.0T using Monte Carlo modeling. Competency of such model to predict R_2^*-iron relationship has previously been demonstrated [64]. In this research, we have modified the model and simulated steatosis to explore R_2^*-FF relationship as well as prediction of FF and R_2^* at different field strengths using multi-spectral fat-water models.

Monte Carlo simulation is employed by modeling possible magnetic field inhomogeneities and mobility of water protons in liver. Water proton's mobility is considered as free random isotropic movement across the simulated geometry which causes change in angle to the magnetic axis and distance from the surrounding FDs resulting in random effect of magnetic field from FDs. To mimic realistic magnetic field inhomogeneities, spheres representing FDs are placed as described in Chapter 4. Rather than choosing average radius for the spheres, radii are chosen from a distribution representing the size of FDs extracted from liver biopsy images. All of these affects the total accumulated phase and consequently helps in simulating realistic MRI signal.

Materials and Methods

Virtual liver environment was created using the relationships generated in Chapter 4. FDs were placed in the liver volume using random and regional anisotropy with NN analysis-based distributions. The following were the relationships between GDF parameters and FFs derived in Chapter 4.

Table 1. Equations representing FD morphology

FD Features	Equation	m	c	R^2
Radius	$\beta = m * FF + c$	0.0809	0.3188	0.49
	$\gamma = m * \beta + c$	-13.254	23.144	0.82
NN Distance	$\beta = m * FF + c$	-0.7777	10.259	0.52
	$\gamma = m * \beta + c$	-0.8583	13.116	0.73
Regional Anisotropy	$\beta = m * FF + c$	0.009	-0.0049	0.27
	$\gamma = m * e^{\beta * c}$	3.5949	-18.98	0.56

A total of 10,000 water protons were distributed randomly in the generated liver volume. The protons were allowed to perform three-dimensional Brownian motion but they were restricted to pass through the FDs. As the protons moved freely, they accumulated phase depending on their movement because their phase would be affected by their position relative to FDs. Water and fat signals were calculated separately, and total signal was computed by the superposition of signals from all the protons. The computerized mathematical model to simulate MRI signal has been discussed below.

Monte Carlo Model for MRI Signal Synthesis and R_2^* Analysis

The magnetic dipole field equation for each FD is calculated using,

$$\Delta B(r, \theta) = \frac{B_0}{3} \chi \left(\frac{R}{r}\right)^3 (3 \cos^2 \theta - 1) \qquad (1)$$

where B0 is the applied magnetic field, χ is the FD susceptibility, R is the sphere radius, r is the radial distance between the center and the observation point and θ is the azimuthal angle to the

magnetic axis. A total of 10,000 water protons were distributed randomly in the liver volume and their mobility was characterized by Brownian motion with mean displacement given by,

$$\sigma = \sqrt{2D\delta} \qquad (2)$$

where D is the diffusion coefficient (D=0 for FD/iron and 0.76 μm^2/ms for water protons in human liver ([65]) and δ is the time-step, which was taken as 0.5μs. The simulation was continued for 15ms and total phase accrual, for each proton, at time step t was given by,

$$\emptyset(t) = \gamma\delta \sum_{i=1}^{t}\left(B_0 + \Delta B(p(i))\right) \qquad (3)$$

where γ =2.675*10^8 rads^{-1}T^{-1} is the gyromagnetic ratio and $p(i)$ is the proton's position at ith time-step. The phase was assumed same for fat and water protons and the complex signal for a single proton was computed as,

$$S_W(t) = S(0)e^{-tR2_0+j\emptyset(t)} \qquad (4)$$

$$S_F(t) = S(0)\left(\sum_{p=1}^{P}\alpha_p e^{j2\pi f_{F,p}t}\right)e^{-tR2_0+j\emptyset(t)} \qquad (5)$$

where R2$_0$ is the relaxation in normal liver and was empirically assumed to be 20s^{-1} at 1.5T and 35s^{-1} at 3.0T, $f_{F,p}$ are the frequencies for the multi-peak fat spectra relative to water peak and α_p are the relative amplitudes of the fat signal. The total synthesized signal was obtained by the superposition of signals from all protons,

$$S(t) = S_w(t) + S_F(t) \qquad (6)$$

The MRI signal relaxation and FF for different steatosis ranges was calculated using multi-spectral fat-water techniques by implementing it on the complex total synthesized signal. The NLSQ model was implemented from the ISMRM Fat-Water Toolbox (FWT) that estimates the B0 field map with the application of the graph cut algorithm. It assumes a single R_2^* for water and fat peaks and uses published values for the relative frequencies of both the peaks, and for the relative amplitudes of the lipid peaks [66]. The Auto Regressive Moving Average Model (ARMA)

was implemented as an iterative approach, similar to [67], starting with the maximum number of fat

peaks (6 peaks) plus a water peak (i.e. 7 peaks) and reducing the number of peaks iteratively

until the frequencies of the detected lipid peaks fell within the range of the reported relative

frequencies ($\pm$ 0.5 ppm) [66].

Comparison with true relaxivity

The R_2^* value predicted by the simulation using different R_2^* models at different FFs were

compared against the in vivo R_2^*-FF calibration curve at 3.0T [68] using Bland Altman plot to

determine the effect of fat on R_2^*.

Results

Magnitude Signal

Figure 1 shows the difference in synthesized signals generated at 1.5T and 3.0T for 12% FF

and $\chi = 0.3$ ppm where the FDs were placed based on regional anisotropy with NN distribution

of FDs. The signals had steeper decay at 3.0T compared to 1.5T because of increase in magnetic

field strength. The plot of the total signal showed that fat and water were in phase for every

4.6ms at 1.5T and 2.3ms at 3.0T (i.e. 4.6ms, 9.2ms, 13.4ms, etc. at 1.5T and 2.3ms, 4.6ms,

6.9ms, etc. at 3.0T). Also, it depicted that the signals had opposed phase starting at 2.3ms and

1.15ms at 1.5T and 3.0T respectively. These Echo Time (TE) values match the known values for

corresponding field strengths.

Figure 2 compares the total synthesized signal (magnitude only) between random distribution

and regional anisotropy with inter-particle distance-based distribution for 12% FF, $\chi=0.3$ppm at

1.5T and 3.0T. The signal showed similar pattern for both the distribution at 1.5T throughout the

simulation time whereas the signal at 3.0T demonstrated steeper slope for regional anisotropy

with NN distribution compared to random distribution in the later time-steps. Figure 3 plots total

synthesized signal at 1.5T and 3.0T for both types of distribution of FDs to differentiate the

signal at various FF (5%, 8% and 12%). As FFs increased, the amplitude of fat-water oscillations

increased as predicted.
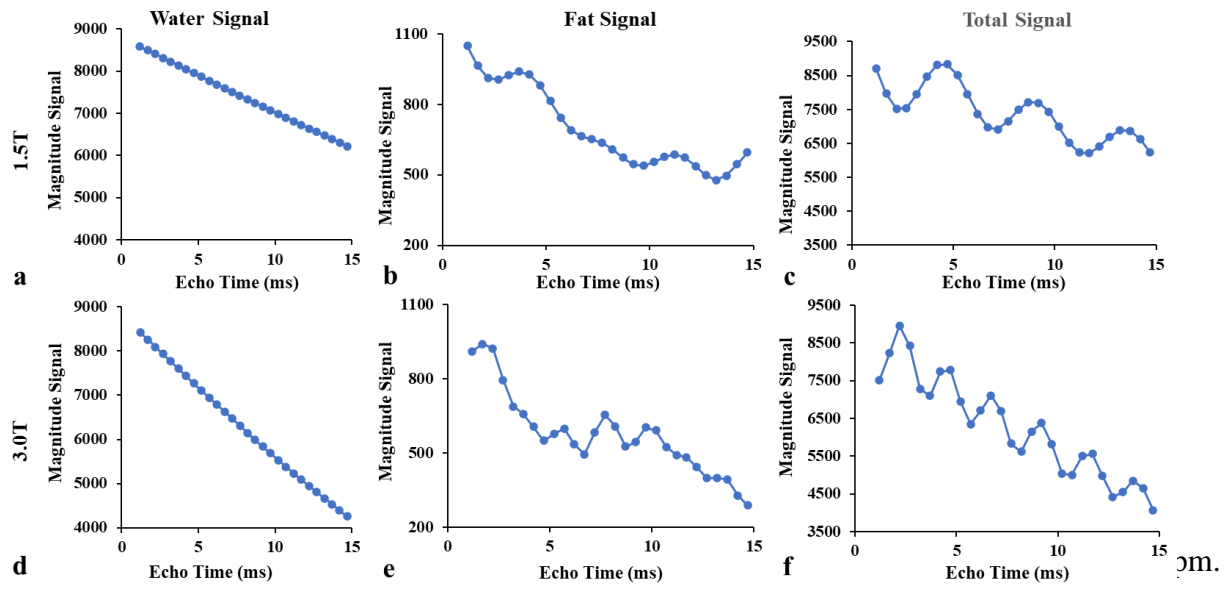
a-c represents 1.5T and d-f represents 3.0T. The TE values matched that of published results.
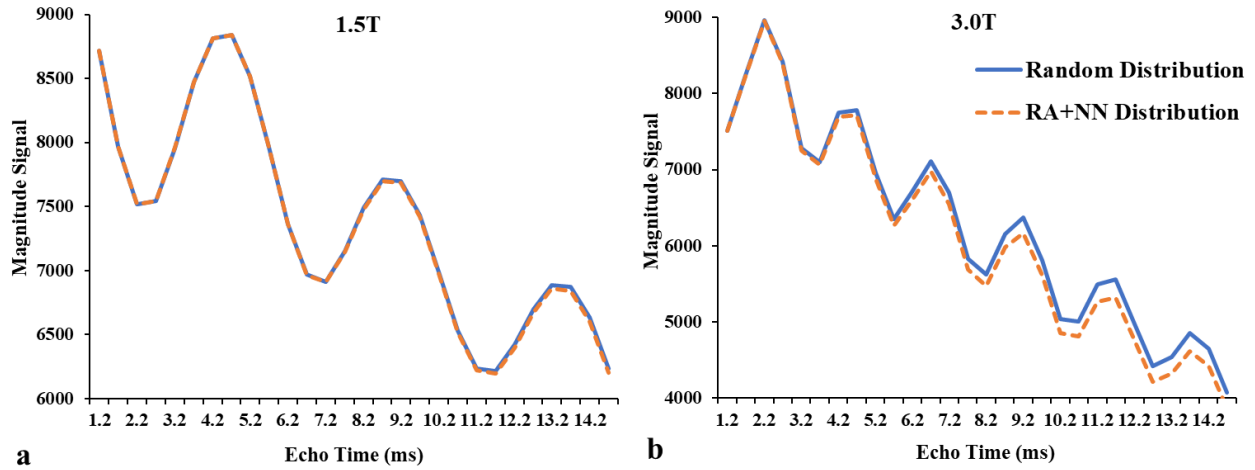
Figure 5-2. Random Distribution vs RA+NN based distribution of FDs using total synthesized magnitude signal for 12% FF and χ =0.3 ppm at 1.5T (a), and 3T (b). The signal decays are similar for both distributions at 1.5T but RA+NN distribution is slightly faster at 3 T.
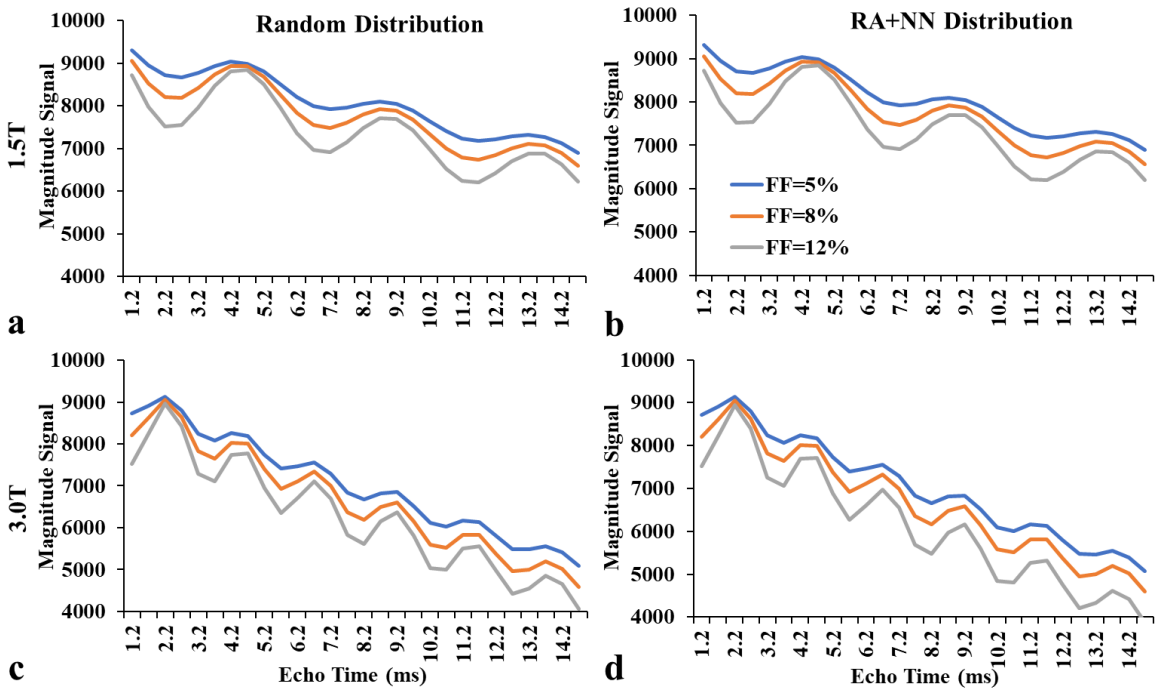
Figure 5-3. Total synthesized signal for different FFs (5%, 8% and 12%), $\chi = 0.3$ppm and both FD distributions at 1.5T and 3T. (a) Random Distribution at 1.5T, (b) RA+NN based distribution at 1.5T, (c) Random Distribution at 3.0T and (d) RA+NN based distribution at 3.0T.

MRI Relaxivity analysis

The relaxivity depends upon the susceptibility of fat. BA analysis for water R_2^* predictions at different susceptibility ranged from -0.3 to 1.4 ppm with respect to in vivo calibration obtained from patients with the absence of iron overload at 3.0T [68]is summarized in Table 2. Overall, the analysis showed that the predictions were evenly distributed around the bias (the mean difference) for the models regardless of the distribution. Both models have bias closest to 0 and thin width of limits of agreement (LOA) for $\chi = 0.4$ppm for random distribution. Among them FWT showed excellent prediction with mean difference of 1.0s^{-1} (SD=0.9s^{-1}) between reference and predicted R_2^* value. For regional anisotropy with NN based distribution, ARMA model produced best outcome with bias = 0.2s^{-1} (SD=0.5s^{-1}) for $\chi = 0.3$ppm. The predicted susceptibility of 0.3ppm is within the 95% CI of the in-vivo susceptibility value 0.10 ± 0.14ppm [69]. So, for rest of the paper susceptibility of FD is considered as 0.3ppm.

Figure 4 plots the water relaxivity estimated by ARMA and FWT model for different FF at 1.5T and 3.0T for random and regional anisotropy with NN based placement of FDs. The plot depicts that the R_2^* of water increases linearly with FF. For 3.0T, the predicted relaxivity values were within 95% CI and regional anisotropy with NN based distribution of FDs agreed more with the in-vivo calibration as shown by BA analysis (Table 2). Generally, ARMA predicted higher R_2^* value as compared to FWT. Similarly, water R_2^* value predicted for regional anisotropy with NN based distribution is higher than that for random distribution of FDs which brings it to only 0.2s^{-1} below the in-vivo calibration from 1.5s^{-1}, according to BA analysis.

Figure 5 shows fat-R_2^* estimated by ARMA model for both distribution of FDs at 1.5T and 3.0T. FWT did not predict R_2^* value for fat because it assumes single relaxation for both fat and water. At lower field strength, the relaxivity of fat did not show any pattern but at 3.0T linear

trend was observed similar to water-R_2^*. The fat relaxivity also demonstrated pattern similar to R_2^* of water for regional anisotropy with NN based distribution where fat-R_2^* is generally higher than that for random distribution of FDs.

Table 2. Bland-Altman analysis between R_2^* values predicted using both models at different susceptibilities versus R_2^* values obtained from the in vivo calibration at 3T.

χ (ppm)	R_2^* Models	Random distribution		RA+NN based distribution	
		Bias (s^{-1})	SD (s^{-1})	Bias (s^{-1})	SD (s^{-1})
-0.3	ARMA	1.4	0.8	0.3	0.5
	FWT	2.1	1.2	0.7	0.7
-0.2	ARMA	3.6	2.0	2.8	1.3
	FWT	3.8	2.3	3.2	1.8
-0.1	ARMA	5.1	2.8	4.9	2.6
	FWT	4.6	3.0	4.6	3.0
0.1	ARMA	5.0	2.7	4.9	2.6
	FWT	4.6	3.0	4.6	3.0
0.2	ARMA	3.5	1.9	2.9	1.4
	FWT	3.8	2.3	3.2	1.8
0.3	ARMA	1.5	0.8	0.2	0.5
	FWT	2.1	1.2	0.7	0.7
0.4	ARMA	-1.2	0.7	-3.3	2.5
	FWT	-1.0	0.9	-3.0	2.4
0.5	ARMA	-1.4	2.4	-7.1	4.8
	FWT	-4.0	2.0	-6.8	4.7
1	ARMA	-22.2	12.0	-26.2	15.8
	FWT	-21.9	12.1	-26.2	15.7
1.4	ARMA	-35.9	19.7	-38.4	22.1
	FWT	-35.9	19.5	-38.2	22.3
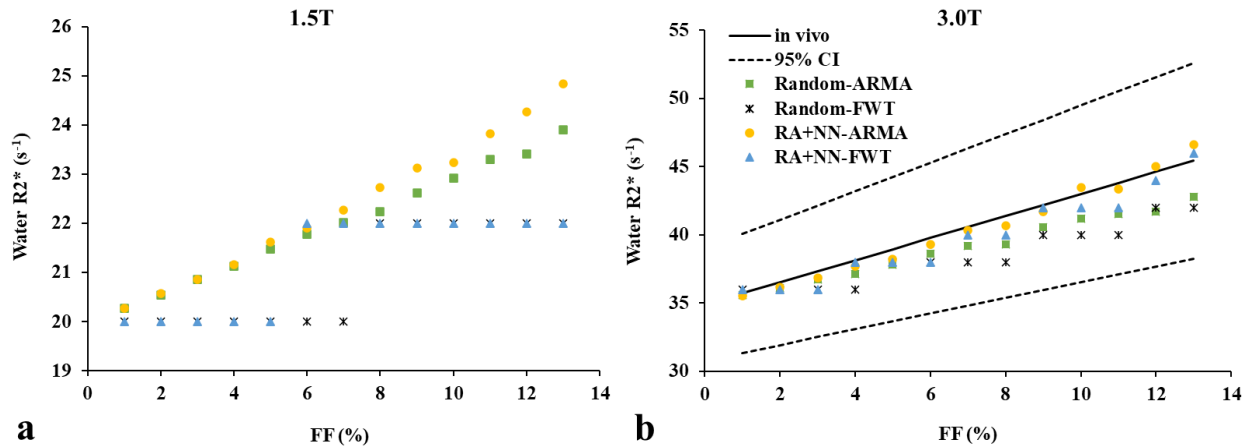
Figure 5-4. Predicted water relaxivities for different R_2^* models for 0-13% FF and $\chi = 0.3$ppm at 1.5T and 3.0T. Overall, R_2^* showed linear increment with FF. Regional Anisotropy with NN distribution showed higher degree of agreement with in-vivo calibration.
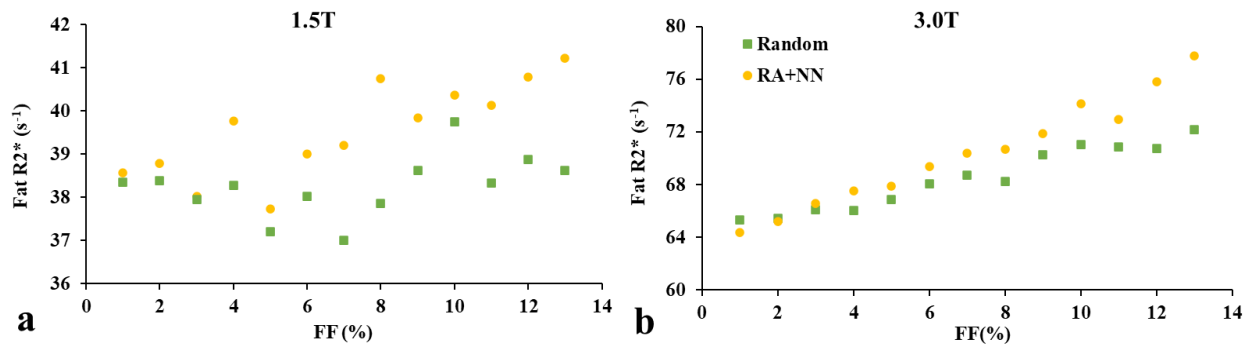
Figure 5-5. Different R_2^* models predicted fat relaxivities at 0-13% FF and $\chi = 0.3$ppm at 1.5T and 3.0T. No pattern was seen at 1.5T but linear trend could be seen at 3.0T.

FF analysis

Figure 6 demonstrates a comparison of FF predicted from R_2^* models with simulated FF for both distributions of FDs at 1.5T and 3.0T. The dotted line shows the line of agreement between them. ARMA model underestimated the FF values at 1.5T and overestimated it at 3.0T. Comparatively, FWT showed greater agreement with the simulated FF for all analyzed cases. This plot shows that both the relaxivity models predict FF with high degree of accuracy.

47
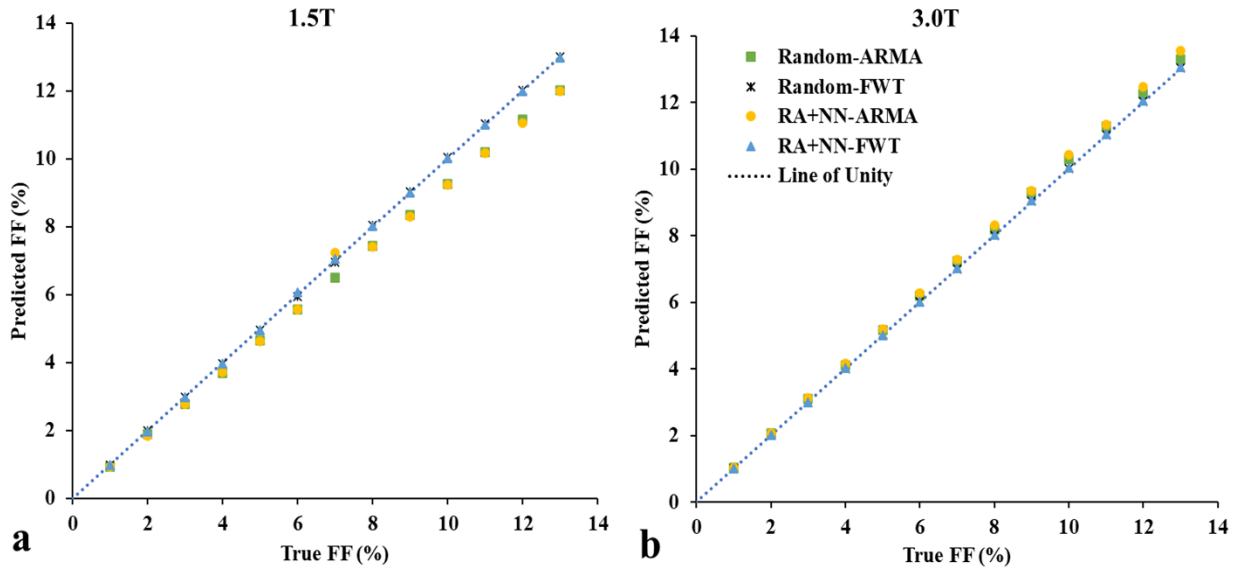
Figure 5-6. Comparison of predicted FF with simulated FF for both distributions and $\chi = 0.3$ppm at 1.5T and 3.0T. The dotted line is the line of unity which shows the point where the two values will be equal. FWT predicted excellent FF result for both distribution of FDs. ARMA seem to estimate lower FF values at 1.5T and higher FF values at 3.0T.

Discussion and Limitations

In this work, we used a Monte Carlo model to synthesize MRI signal and analyze the FF as well as relaxivity of fat and water at different field strengths using FWT and ARMA models. The presence of lipid droplets impacts R_2^* of MRI signal. Although the magnetic susceptibility of fat is relatively small in comparison with iron, it can generate small field inhomogeneity which can increase the signal decay rate resulting to higher R_2^* [70]. Our work demonstrates that there was increase in decay rate of MRI signal with increase in FF which suggests that fat produces field inhomogeneity.

There is a strong cooccurrence of NAFLD along with hyperferritinemia and mild iron overload [71]. The susceptibility of iron is very high compared to that of fat. So, quantifying fat susceptibility in the presence of iron is difficult and proper analysis of fat susceptibility has not been done yet.

For estimating the susceptibility of fat, we analyzed the relaxivity of fat and water as well as FF at different fat susceptibilities -0.1 to 0.5 ppm and 1 ppm. Then, evaluated i) $R_{2,W}^*$ with in vivo calibration and ii) predicted FF with true simulated FF at those susceptibilities. The BA analysis and line of unity analysis produced excellent result for $\chi = 0.3$ ppm which is within 95% CI of the in-vivo calibration (0.10±0.14ppm) [69]. Hence, this method was able to estimate the susceptibility of fat with acceptable accuracy. Susceptibility of 0.5ppm predicted by Monte Carlo modeling is reported in [72]. The difference might be because they have simulated FDs with constant radius using random distribution.

The R_2^* values of water predicted by ARMA and FWT model were within the 95% confidence bound for both distributions of FDs but the values for regional anisotropy with nearest neighbor distribution of FDs were comparatively closer to the in-vivo calibration at 3.0T for $\chi = 0.3$ ppm. Also, this result was validated by BA analysis. This shows that both the distributions of FDs were able to simulate hepatic steatosis and mimic MRI signal with acceptable accuracy (BA analysis, random distribution: 1.5±0.8 and regional anisotropy with NN distribution: 0.2±0.5) but the distribution with regional anisotropy and nearest neighbor was superior by being able to simulate in-vivo characteristic of FDs.

The ARMA models consider different R_2^* for fat and water and should be able to estimate the FF with higher accuracy as compared to FWT (single R_2^*) but it is not stable at low FF and FF quantification accuracy decreases [52]. This work supports the result published in [52,73] and shows that single R_2^* model is better for quantifying FF. However, our findings related to different relaxivity of fat and water (29.97±0.63 s⁻¹) for ARMA model contradicts the result reported in [52]. They observed that both relaxivities were very similar with mean difference of 0.95±8.28 s⁻¹. We found similar $R_{2,F}^*$ and $R_{2,W}^*$ (0.46±0.88) for $\chi = \pm0.1$ ppm where ARMA peak model was able to

identify all 6 peaks of lipid but $R_{2,W}^*$ predicted at $\chi = \pm 0.1$ was not within 95% CI of in-vivo $R_{2,W}^*$ calibration. The difference for $\chi = 0.3$ppm might be because ARMA model was able to identify only 2 fat peaks.

In the absence of high FF, the simulation could not mimic severe hepatic steatosis but this study showed that the information of size of FDs, inter-particle distance and regional anisotropy was useful to mimic steatosis and analyze R_2^* within 95% CI of the in vivo calibration. This showed the feasibility of Monte Carlo modeling to mimic fat accumulation in liver. Simulation of fat deposition in other organs could be achieved by using similar data about them. In addition, it can be used to mimic steatosis of organs where liver biopsy is not possible by gathering that information from autopsy specimens.

In summary, complete knowledge of size and location of FDs is required to mimic steatosis. We were able to predict in vivo human water relaxivity within 95% CI using the radius and distance between closest FD neighbor from mice liver sample. In addition, we used it to estimate the susceptibility of fat in liver. The result can further be improved by conducting the experiment with human liver sample that covers entire clinical range of FF and improving the ARMA 7 peak model to identify all 6 lipid peaks.

Chapter 6 Conclusion

MRI provides a non-invasive tool to monitor hepatic steatosis [3,4,48] but it is still under research. Studies have used single and dual R_2^* to quantify FF but there is no common agreement about which R_2^* model is superior to other. R_2^*-FF relationship must be analyzed further to increase the clinical acceptance of MRI. It is difficult, tedious and expensive to recalibrate the R_2^* estimates in large patient population representing entire FF clinical range.

The primary objective of our study was to develop an alternative approach to recalibrate the FF-R_2^* relationship and to determine the accuracy of single and dual R_2^* models. Our hypothesis states that the in vivo FF-relaxivity relationship can be estimated using Monte Carlo modeling provided the morphology, location and susceptibility of FDs, water proton mobility in tissue and R_2^* model. This approach can reduce or eliminate the need of patient population for recalibration. In addition, it can be used to study other phenomenon related to steatosis.

Original Contributions

The innovations of this study are:

1. Automatic segmentation of FDs has been done previously [55-57] but the morphology and distribution pattern of FDs based on FF have never been quantified. This study has analyzed those characteristics of FDs and developed a statistical model to represent them. This led a foundation to simulate hepatic steatosis with desired FF. Also, it provided information about the size and distribution of FDs in liver.

2. Monte Carlo modeling for mimicking steatosis with properties of FDs extracted from liver biopsy samples is used for the first time. In this work, we used the simulation to study the effect of fat deposition on MRI relaxivity for different field strengths and R_2^* models. Fat

deposition differs with tissue so we believe that tissue specific statistical models can be generated and this approach can be used to build tissue specific simulations.

Findings

Our work has demonstrated the potential of using computerized technique to examine the FF-R_2^* calibration. The size and inter-particle distance of lipid droplets for different FF was obtained from liver biopsy specimens of mice. Gamma Distribution Function was used to represent those characteristics. GDF proved to be a suitable fit for modeling them by showing expected variations corresponding to the features of FDs. For example: GDF showed increment in size of FDs as we move to higher FF which is a well implied result. The larger volume of the droplets contributed to increase in FF. In addition, the shape and scale parameters of GDF showed good correlation with FF. Hence, we can conclude that GDF was able to characterize the FDs appropriately and demonstrated to be a good choice.

With the simulation of hepatic steatosis using statistical models, Monte Carlo modeling was used to generate MRI signal in the virtual environment. We were able to generate realistic MRI signals and analyze the effect of FDs on the MRI relaxivity. We used single as well as dual R_2^* models for the analysis. The R_2^* of both fat and water was found to increase linearly with FF which agreed with published result [70]. The in-phase and opposed-phase cycle of the simulated signals matched that of known values. Also, the relaxivity values of water at 3.0T field strength were within 95% confidence bound of in-vivo calibration and had mean offset of -1.5±0.8 and 0.2±0.5 from true values for random and regional anisotropy with NN distribution respectively. This showed that Monte Carlo modeling successfully simulated the MRI signal in fatty liver. This helped us to examine the susceptibility of fat in liver which is generally convoluted in the presence of iron in human liver. Our experiment estimated the susceptibility of fat as 0.3 ppm.

Also, our research showed that single R_2^* model is more accurate than dual R_2^* model for quantifying FF. The steatosis simulation as well as Monte Carlo modeling can be used for other similar examinations and analysis.

Future Works

We have successfully built a realistic hepatic steatosis 3D model and used it to estimate single and dual R_2^*-FF relationship with acceptable accuracy but there are areas that still need more attention. Some of them are discussed below.

1. The automatic segmentation of FDs from liver biopsy was validated qualitatively but was not cross validated with more rigorous manual segmentation by pathologists such as manual point counting. The cross validation can be used to test the accuracy of the segmentation.

2. The FFs in our liver samples do not cover the entire clinical range 0-50% [74]. This study has shown that realistic liver model can be generated for 0-13% FF. The techniques developed in this study can be used to simulate steatosis for entire clinical range.

3. The relaxivities estimated by the Monte Carlo model are based on the true diffusion coefficient (D) of water in tissues. The value of D depends upon tissue organization and fat-proton interaction. The only published value of D for normal liver is 0.76 ± 0.27 µm^2/ms [65]. The value of D in the presence of fat is not known. The true value of D in fatty tissues can help in accurate calibration of R_2^* values.

4. In this study, we have used mice liver samples and compared the predicted relaxivities with human in vivo calibrations. The prediction of this method can be improved by performing this experiment with human liver specimens. Also, the predicted relaxivities needs to be compared with in vivo calibration at 1.5T.

5. A strong co-occurrence of NAFLD along with hyperferritinemia and mild iron overload has been reported [71]. So, designing models simulating both steatosis and iron-overload can be helpful to study the combined effect of iron and fat on MRI signal.

References

1. Younossi, Z.; Tacke, F.; Arrese, M.; Chander Sharma, B.; Mostafa, I.; Bugianesi, E.; Wai-Sun Wong, V.; Yilmaz, Y.; George, J.; Fan, J. Global perspectives on nonalcoholic fatty liver disease and nonalcoholic steatohepatitis. *Hepatology* **2019***, 69*, 2672-2682.

2. Baršić, N.; Lerotić, I.; Smirčić-Duvnjak, L.; Tomašić, V.; Duvnjak, M. Overview and developments in noninvasive diagnosis of nonalcoholic fatty liver disease. *World Journal of Gastroenterology: WJG* **2012***, 18*, 3945.

3. Idilman, I. S.; Aniktar, H.; Idilman, R.; Kabacam, G.; Savas, B.; Elhan, A.; Celik, A.; Bahar, K.; Karcaaltincaba, M. Hepatic steatosis: quantification by proton density fat fraction with MR imaging versus liver biopsy. *Radiology* **2013***, 267*, 767-775.

4. Tang, A.; Tan, J.; Sun, M.; Hamilton, G.; Bydder, M.; Wolfson, T.; Gamst, A. C.; Middleton, M.; Brunt, E. M.; Loomba, R. Nonalcoholic fatty liver disease: MR imaging of liver proton density fat fraction to assess hepatic steatosis. *Radiology* **2013***, 267*, 422-431.

5. Kühn, J.; Hernando, D.; Muñoz del Rio, A.; Evert, M.; Kannengiesser, S.; Völzke, H.; Mensel, B.; Puls, R.; Hosten, N.; Reeder, S. B. Effect of multipeak spectral modeling of fat for liver iron and fat quantification: correlation of biopsy with MR imaging results. *Radiology* **2012***, 265*, 133-142.

6. Meisamy, S.; Hines, C. D.; Hamilton, G.; Sirlin, C. B.; McKenzie, C. A.; Yu, H.; Brittain, J. H.; Reeder, S. B. Quantification of hepatic steatosis with T1-independent, T2*-corrected MR imaging with spectral modeling of fat: blinded comparison with MR spectroscopy. *Radiology* **2011***, 258*, 767-775.

7. Yokoo, T.; Bydder, M.; Hamilton, G.; Middleton, M. S.; Gamst, A. C.; Wolfson, T.; Hassanein, T.; Patton, H. M.; Lavine, J. E.; Schwimmer, J. B. Nonalcoholic fatty liver disease: diagnostic and fat-grading accuracy of low-flip-angle multiecho gradient-recalled-echo MR imaging at 1.5 T. *Radiology* **2009***, 251*, 67-76.

8. Reeder, S. B.; Robson, P. M.; Yu, H.; Shimakawa, A.; Hines, C. D.; McKenzie, C. A.; Brittain, J. H. Quantification of hepatic steatosis with MRI: the effects of accurate fat spectral modeling. *Journal of Magnetic Resonance Imaging: An Official Journal of the International Society for Magnetic Resonance in Medicine* **2009***, 29*, 1332-1339.

9. Boxerman, J. L.; Hamberg, L. M.; Rosen, B. R.; Weisskoff, R. M. MR contrast due to intravascular magnetic susceptibility perturbations. *Magnetic resonance in medicine* **1995***, 34*, 555-566.

10. Ford, J. C.; Wehrli, F. W. In vivo quantitative characterization of trabecular bone by NMR. *Magnetic resonance in medicine* **1991***, 17*, 543-551.

11. Gillis, P.; Petö, S.; Moiny, F.; Mispelter, J.; Cuenod, C. Proton transverse nuclear magnetic relaxation in oxidized blood: a numerical approach. *Magnetic resonance in medicine* **1995**, *33*, 93-100.

12. Weisskoff, R.; Zuo, C. S.; Boxerman, J. L.; Rosen, B. R. Microscopic susceptibility variation and transverse relaxation: theory and experiment. *Magnetic Resonance in Medicine* **1994**, *31*, 601-610.

13. Coyle, E. F. Fat metabolism during exercise. *Sports Science Exchange* **1995**, *8*, 59.

14. Rapoport, S. I.; Ramadan, E.; Basselin, M. Docosahexaenoic acid (DHA) incorporation into the brain from plasma, as an in vivo biomarker of brain DHA metabolism and neurotransmission. *Prostaglandins Other Lipid Mediat.* **2011**, *96*, 109-113.

15. Finkelstein, E. A.; Khavjou, O. A.; Thompson, H.; Trogdon, J. G.; Pan, L.; Sherry, B.; Dietz, W. Obesity and severe obesity forecasts through 2030. *Am. J. Prev. Med.* **2012**, *42*, 563-570.

16. Kahn, B. B.; Flier, J. S. Obesity and insulin resistance. *J. Clin. Invest.* **2000**, *106*, 473-481.

17. Dash, A.; Figler, R. A.; Sanyal, A. J.; Wamhoff, B. R. Drug-induced steatohepatitis. *Expert opinion on drug metabolism & toxicology* **2017**, *13*, 193-204.

18. Khan, A. Z.; Morris-Stiff, G.; Makuuchi, M. Patterns of chemotherapy-induced hepatic injury and their implications for patients undergoing liver resection for colorectal liver metastases. *J. Hepatobiliary. Pancreat.* **2009**, *16*, 137-144.

19. Maor, Y.; Malnick, S. Liver injury induced by anticancer chemotherapy and radiation therapy. *International journal of hepatology* **2013**, *2013*.

20. Raptis, D. A.; Fischer, M. A.; Graf, R.; Nanz, D.; Weber, A.; Moritz, W.; Tian, Y.; Oberkofler, C. E.; Clavien, P. MRI: the new reference standard in quantifying hepatic steatosis? *Gut* **2012**, *61*, 117-127.

21. Anstee, Q. M.; Day, C. P. Epidemiology, Natural History, and Evaluation of Nonalcoholic Fatty Liver Disease. In *Zakim and Boyer's Hepatology*Elsevier: 2018; pp 391-405. e3.

22. Zezos, P.; Renner, E. L. Liver transplantation and non-alcoholic fatty liver disease. *World journal of gastroenterology: WJG* **2014**, *20*, 15532.

23. Tolman, K. G.; Dalpiaz, A. S. Treatment of non-alcoholic fatty liver disease. *Therapeutics and clinical risk management* **2007**, *3*, 1153.

24. Petersen, K. F.; Dufour, S.; Befroy, D.; Lehrke, M.; Hendler, R. E.; Shulman, G. I. Reversal of nonalcoholic hepatic steatosis, hepatic insulin resistance, and hyperglycemia by moderate weight reduction in patients with type 2 diabetes. *Diabetes* **2005**, *54*, 603-608.

25. Suzuki, A.; Lindor, K.; St Saver, J.; Lymp, J.; Mendes, F.; Muto, A.; Okada, T.; Angulo, P. Effect of changes on body weight and lifestyle in nonalcoholic fatty liver disease. *J. Hepatol.* **2005***, 43*, 1060-1066.

26. Huang, M. A.; Greenson, J. K.; Chao, C.; Anderson, L.; Peterman, D.; Jacobson, J.; Emick, D.; Lok, A. S.; Conjeevaram, H. S. One-year intense nutritional counseling results in histological improvement in patients with non-alcoholic steatohepatitis: a pilot study. *Am. J. Gastroenterol.* **2005***, 100*, 1072-1081.

27. Angulo, P. NAFLD, obesity, and bariatric surgery. *Gastroenterology* **2006***, 130*, 1848-1852.

28. Mattar, S. G.; Velcu, L. M.; Rabinovitz, M.; Demetris, A. J.; Krasinskas, A. M.; Barinas-Mitchell, E.; Eid, G. M.; Ramanathan, R.; Taylor, D. S.; Schauer, P. R. Surgically-induced weight loss significantly improves nonalcoholic fatty liver disease and the metabolic syndrome. *Ann. Surg.* **2005***, 242*, 610.

29. Clark, J. M.; Alkhuraishi, A. R.; Solga, S. F.; Alli, P.; Diehl, A. M.; Magnuson, T. H. Roux-en-Y gastric bypass improves liver histology in patients with non-alcoholic fatty liver disease. *Obes. Res.* **2005***, 13*, 1180-1186.

30. Dixon, J. B.; Bhathal, P. S.; Hughes, N. R.; O'Brien, P. E. Nonalcoholic fatty liver disease: improvement in liver histological analysis with weight loss. *Hepatology* **2004***, 39*, 1647-1654.

31. Sabuncu, T.; Nazligul, Y.; Karaoglanoglu, M.; Ucar, E.; Kilic, F. B. The effects of sibutramine and orlistat on the ultrasonographic findings, insulin resistance and liver enzyme levels in obese patients with non-alcoholic steatohepatitis. *Romanian journal of gastroenterology* **2003***, 12*, 189-192.

32. Zelber-Sagi, S.; Kessler, A.; Brazowsky, E.; Webb, M.; Lurie, Y.; Santo, M.; Leshno, M.; Blendis, L. M.; Halpern, Z.; Oren, R. In *In Randomized placebo-controlled trial of orlistat for the treatment of patients with non alcoholic fatty liver disease (NAFLD);* Hepatology; JOHN WILEY & SONS INC 111 RIVER ST, HOBOKEN, NJ 07030 USA: 2004; Vol. 40, pp 237A.

33. Castera, L.; Vilgrain, V.; Angulo, P. Noninvasive evaluation of NAFLD. *Nature reviews Gastroenterology & hepatology* **2013***, 10*, 666-675.

34. Stern, C.; Castera, L. Non-invasive diagnosis of hepatic steatosis. *Hepatology international* **2017***, 11*, 70-78.

35. Bydder, G. M.; Kreel, L.; Chapman, R. W.; Harry, D.; Sherlock, S.; Bassan, L. Accuracy of computed tomography in diagnosis of fatty liver. *Br. Med. J.* **1980***, 281*, 1042.

36. Piekarski, J.; Goldberg, H. I.; Royal, S. A.; Axel, L.; Moss, A. A. Difference between liver and spleen CT numbers in the normal adult: its usefulness in predicting the presence of diffuse liver disease. *Radiology* **1980***, 137*, 727-729.

37. Mehta, S. R.; Thomas, E. L.; Bell, J. D.; Johnston, D. G.; Taylor-Robinson, S. D. Non-invasive means of measuring hepatic fat content. *World journal of gastroenterology: WJG* **2008***, 14*, 3476.

38. Park, S. H.; Kim, P. N.; Kim, K. W.; Lee, S. W.; Yoon, S. E.; Park, S. W.; Ha, H. K.; Lee, M.; Hwang, S.; Lee, S. Macrovesicular hepatic steatosis in living liver donors: use of CT for quantitative and qualitative assessment. *Radiology* **2006***, 239*, 105-112.

39. Idilman, I. S.; Keskin, O.; Celik, A.; Savas, B.; Halil Elhan, A.; Idilman, R.; Karcaaltincaba, M. A comparison of liver fat content as determined by magnetic resonance imaging-proton density fat fraction and MRS versus liver histology in non-alcoholic fatty liver disease. *Acta Radiol.* **2016***, 57*, 271-278.

40. Reeder, S. B.; Cruite, I.; Hamilton, G.; Sirlin, C. B. Quantitative assessment of liver fat with magnetic resonance imaging and spectroscopy. *Journal of magnetic resonance imaging* **2011***, 34*, 729-749.

41. Permutt, Z.; Le, T.; Peterson, M. R.; Seki, E.; Brenner, D. A.; Sirlin, C.; Loomba, R. Correlation between liver histology and novel magnetic resonance imaging in adult patients with non-alcoholic fatty liver disease–MRI accurately quantifies hepatic steatosis in NAFLD. *Aliment. Pharmacol. Ther.* **2012***, 36*, 22-29.

42. Hines, C. D.; Frydrychowicz, A.; Hamilton, G.; Tudorascu, D. L.; Vigen, K. K.; Yu, H.; McKenzie, C. A.; Sirlin, C. B.; Brittain, J. H.; Reeder, S. B. T1 independent, T2* corrected chemical shift based fat–water separation with multi-peak fat spectral modeling is an accurate and precise measure of hepatic steatosis. *Journal of magnetic resonance imaging* **2011***, 33*, 873-881.

43. Siegelman, E. S.; Rosen, M. A. In *In Imaging of hepatic steatosis;* Seminars in Liver Disease; Copyright© 2001 by Thieme Medical Publishers, Inc., 333 Seventh Avenue, New …: 2001; Vol. 21, pp 71.

44. Dixon, W. T. Simple proton spectroscopic imaging. *Radiology* **1984***, 153*, 189-194.

45. Lee, J. K.; Dixon, W. T.; Ling, D.; Levitt, R. G.; Murphy Jr, W. A. Fatty infiltration of the liver: demonstration by proton spectroscopic imaging. Preliminary observations. *Radiology* **1984***, 153*, 195-201.

46. Heiken, J. P.; Lee, J. K.; Dixon, W. T. Fatty infiltration of the liver: evaluation by proton spectroscopic imaging. *Radiology* **1985***, 157*, 707-710.

47. Reeder, S. B.; Sirlin, C. B. Quantification of liver fat with magnetic resonance imaging. *Magnetic Resonance Imaging Clinics* **2010**, *18*, 337-357.

48. Bannas, P.; Kramer, H.; Hernando, D.; Agni, R.; Cunningham, A. M.; Mandal, R.; Motosugi, U.; Sharma, S. D.; Munoz del Rio, A.; Fernandez, L. Quantitative magnetic resonance imaging of hepatic steatosis: Validation in ex vivo human livers. *Hepatology* **2015**, *62*, 1444-1455.

49. Yu, H.; McKenzie, C. A.; Shimakawa, A.; Vu, A. T.; Brau, A. C.; Beatty, P. J.; Pineda, A. R.; Brittain, J. H.; Reeder, S. B. Multiecho reconstruction for simultaneous water-fat decomposition and T2* estimation. *Journal of Magnetic Resonance Imaging: An Official Journal of the International Society for Magnetic Resonance in Medicine* **2007**, *26*, 1153-1161.

50. Chebrolu, V. V.; Hines, C. D.; Yu, H.; Pineda, A. R.; Shimakawa, A.; McKenzie, C. A.; Samsonov, A.; Brittain, J. H.; Reeder, S. B. Independent estimation of T* 2 for water and fat for improved accuracy of fat quantification. *Magnetic Resonance in Medicine: An Official Journal of the International Society for Magnetic Resonance in Medicine* **2010**, *63*, 849-857.

51. Hernando, D.; Liang, Z.; Kellman, P. Chemical shift-based water/fat separation: A comparison of signal models. *Magnetic resonance in medicine* **2010**, *64*, 811-822.

52. Horng, D. E.; Hernando, D.; Hines, C. D.; Reeder, S. B. Comparison of R2* correction methods for accurate fat quantification in fatty liver. *Journal of Magnetic Resonance Imaging* **2013**, *37*, 414-422.

53. Zaitoun, A. M.; Al Mardini, H.; Awad, S.; Ukabam, S.; Makadisi, S.; Record, C. O. Quantitative assessment of fibrosis and steatosis in liver biopsies from patients with chronic hepatitis C. *J. Clin. Pathol.* **2001**, *54*, 461-465.

54. Boyles, T. H.; Johnson, S.; Garrahan, N.; Freedman, A. R.; Williams, G. T. A validated method for quantifying macrovesicular hepatic steatosis in chronic hepatitis C. *Analytical and quantitative cytology and histology* **2007**, *29*, 244-250.

55. Sethunath, D.; Morusu, S.; Tuceryan, M.; Cummings, O. W.; Zhang, H.; Yin, X.; Vanderbeck, S.; Chalasani, N.; Gawrieh, S. Automated assessment of steatosis in murine fatty liver. *PloS one* **2018**, *13*.

56. Vanderbeck, S.; Bockhorst, J.; Komorowski, R.; Kleiner, D. E.; Gawrieh, S. Automatic classification of white regions in liver biopsies by supervised machine learning. *Hum. Pathol.* **2014**, *45*, 785-792.

57. Nativ, N. I.; Chen, A. I.; Yarmush, G.; Henry, S. D.; Lefkowitch, J. H.; Klein, K. M.; Maguire, T. J.; Schloss, R.; Guarrera, J. V.; Berthiaume, F. Automated image analysis

method for detecting and quantifying macrovesicular steatosis in hematoxylin and eosin-stained histology images of human livers. *Liver Transplantation* **2014***, 20*, 228-236.

58. Marsman, H.; Matsushita, T.; Dierkhising, R.; Kremers, W.; Rosen, C.; Burgart, L.; Nyberg, S. L. Assessment of donor liver steatosis: pathologist or automated software? *Hum. Pathol.* **2004***, 35*, 430-435.

59. Roullier, V.; Cavaro-Menard, C.; Guillaume, C.; Aube, C. In *In Fuzzy algorithms to extract vacuoles of steatosis on liver histological color images;* 2007 29th Annual International Conference of the IEEE Engineering in Medicine and Biology Society; IEEE: 2007; , pp 5575-5578.

60. Liquori, G. E.; Calamita, G.; Cascella, D.; Mastrodonato, M.; Portincasa, P.; Ferri, D. An innovative methodology for the automated morphometric and quantitative estimation of liver steatosis. *Histol. Histopathol.* **2009**.

61. Otsu, N. A threshold selection method from gray-level histograms. *IEEE Trans. Syst. Man Cybern.* **1979***, 9*, 62-66.

62. Homeyer, A.; Schenk, A.; Arlt, J.; Dahmen, U.; Dirsch, O.; Hahn, H. K. Fast and accurate identification of fat droplets in histological images. *Comput. Methods Programs Biomed.* **2015***, 121*, 59-65.

63. Vanderbeck, S.; Bockhorst, J.; Kleiner, D.; Komorowski, R.; Chalasani, N.; Gawrieh, S. Automatic quantification of lobular inflammation and hepatocyte ballooning in nonalcoholic fatty liver disease liver biopsies. *Hum. Pathol.* **2015***, 46*, 767-775.

64. Ghugre, N. R.; Wood, J. C. Relaxivity-iron calibration in hepatic iron overload: probing underlying biophysical mechanisms using a Monte Carlo model. *Magnetic resonance in medicine* **2011***, 65*, 837-847.

65. Yamada, I.; Aung, W.; Himeno, Y.; Nakagawa, T.; Shibuya, H. Diffusion coefficients in abdominal organs and hepatic lesions: evaluation with intravoxel incoherent motion echo-planar MR imaging. *Radiology* **1999***, 210*, 617-623.

66. Hamilton, G.; Yokoo, T.; Bydder, M.; Cruite, I.; Schroeder, M. E.; Sirlin, C. B.; Middleton, M. S. In vivo characterization of the liver fat 1H MR spectrum. *NMR Biomed.* **2011***, 24*, 784-790.

67. Tipirneni-Sajja, A.; Krafft, A. J.; Loeffler, R. B.; Song, R.; Bahrami, A.; Hankins, J. S.; Hillenbrand, C. M. Autoregressive moving average modeling for hepatic iron quantification in the presence of fat. *Journal of Magnetic Resonance Imaging* **2019***, 50*, 1620-1632.

68. Hernando, D.; Haufe, W. M.; Hooker, C. A.; Schlein, A.; Wolfson, T.; Artz, N. S.; Reeder, S. B.; Sirlin, C. B. In *In Relationship between liver proton density fat fraction and R2* in the absence of iron overload;* Proc ISMRM; 2015; Vol. 4118.

69. Leporq, B.; Lambert, S. A.; Ronot, M.; Vilgrain, V.; Van Beers, B. E. Simultaneous MR quantification of hepatic fat content, fatty acid composition, transverse relaxation time and magnetic susceptibility for the diagnosis of non-alcoholic steatohepatitis. *NMR Biomed.* **2017***, 30*, e3766.

70. Hernando, D.; Vigen, K. K.; Shimakawa, A.; Reeder, S. B. R mapping in the presence of macroscopic B0 field variations. *Magnetic resonance in medicine* **2012***, 68*, 830-840.

71. Valenti, L.; Rametta, R.; Dongiovanni, P.; Motta, B. M.; Canavesi, E.; Pelusi, S.; Pulixi, E. A.; Fracanzani, A. L.; Fargion, S. The A736V TMPRSS6 polymorphism influences hepatic iron overload in nonalcoholic fatty liver disease. *PLoS One* **2012***, 7*.

72. Changqing Wang, Benjamin Ratliff, Claude Sirlin, Scott Reeder DH Monte Carlo Modeling of Liver MR Signal in the Presence of Fat. International Society for Magnetic Resonance in Medicine. **2018**, 26.

73. Hernando, D.; Liang, Z.; Kellman, P. Chemical shift–based water/fat separation: A comparison of signal models. *Magnetic resonance in medicine* **2010***, 64*, 811-822.

74. Dulai, P. S.; Sirlin, C. B.; Loomba, R. MRI and MRE for non-invasive quantitative assessment of hepatic steatosis and fibrosis in NAFLD and NASH: Clinical trials to clinical practice. *J. Hepatol.* **2016***, 65*, 1006-1016.